Research Article

Haitham Osman, Norah Salem Alsaiari*, Abdelfattah Amari*, and Mohamed A. Tahoon

Synthesis and characterization of a novel ternary magnetic composite for the enhanced adsorption capacity to remove organic dyes

https://doi.org/10.1515/rams-2024-0009
received January 08, 2024; accepted March 11, 2024

Abstract: Using an easy mechanical agitation process at room temperature, a metal–organic framework (MOF) based on metallic Zn(II), organic linker benzene-1,3,5-tricarboxylic acid (Zn-BTC), Fe_3O_4 nanoparticles, and nanocellulose are combined to create a novel composite material called Fe_3O_4/NC/MOF. Various tools were used to characterize the created composite. Congo red, Basic Blue 54 (BB 54), Basic Violet 14 (BV 14), and Acid red 88 (AR 88) dyes were effectively eliminated from water using Fe_3O_4/NC/MOF. A number of variables were investigated, including pH, temperature, contact time, initial dye concentration, and adsorbent dosage. To understand the specific adsorption process, a number of kinetic models were used, including the intra-particle diffusion model, Elovich's kinetic model, pseudo-first-order, and pseudo-second-order kinetic models. The most accurate description of dye sorption kinetics comes from the pseudo-second-order kinetic model. Also, the Langmuir model is more accurate to describe isotherms than Freundlich and Temkin models. Furthermore, thermodynamic parameters were obtained and examined, including enthalpy (ΔH), Gibbs free energy (ΔG), and entropy (ΔS). After four cycles, the Fe_3O_4/NC/MOF demonstrated good recyclability. According to experimental research, this adsorbent is promising to enhance the quality of environmental water that has been tainted with organic dyes.

Keywords: water treatment, adsorption, metal, organic framework

1 Introduction

The problem of water contamination has become increasingly urgent and dangerous as a result of the expansion of international trade and industrial activity, particularly in the leather tanning and textile industries [1,2]. These activities cause large volumes of organic dyes to be released into the environment, which has led to major pollution issues. Since most dyes are synthetic and include aromatic rings, they cannot biodegrade, are mutagenic and carcinogenic, and will not break down if they are dumped into waste streams [3,4]. They may have immediate or long-term effects on organisms that come into contact with them. Water-soluble dyes also absorb or reflect sunlight, preventing the growth of microorganisms [5]. Moreover, even in low quantities, they cause aesthetic pollution and are apparent. Consequently, it is crucial to significantly reduce the color of aquatic systems. To remove contaminants from water, a variety of treatments have been used, including chemical precipitation [6], coagulation [7], membrane filtration [8], adsorption [9,10], microbial degradation [11], and ion exchange [12,13]. Adsorption is one of these treatments that has received a lot of attention due to its easy to use, affordable, and highly effective nature [14,15].

Metal–organic frameworks (MOFs) are one-, two-, or three-dimensional porous crystalline polymer networks made up of metal nodes (metal ions or clusters) attached to multidentate organic linkers [16]. The linkers are then joined by strong covalent connections. Porous coordination networks and porous coordination polymers are other names for MOFs. They exhibit special qualities that go beyond what would be expected from a straightforward combination of these components, in addition to combining the advantageous aspects of organic and inorganic

*** Corresponding author: Norah Salem Alsaiari,** Department of Chemistry, College of Science, Princess Nourah bint Abdulrahman University, P.O. Box 84428, Riyadh 11671, Saudi Arabia, e-mail: nsalsaiari@pnu.edu.sa
*** Corresponding author: Abdelfattah Amari,** Department of Chemical Engineering, College of Engineering, King Khalid University, Abha 61411, Kingdom of Saudi Arabia, e-mail: abdelfattah.amari@enig.rnu.tn
Haitham Osman: Department of Chemical Engineering, College of Engineering, King Khalid University, Abha 61411, Kingdom of Saudi Arabia
Mohamed A. Tahoon: Department of Chemistry, College of Science, King Khalid University, P.O. Box 9004, Abha 61413, Saudi Arabia; Chemistry Department, Faculty of Science, Mansoura University, Mansoura 35516, Egypt

elements. MOFs have drawn particular attention for a variety of applications, including gas separation and storage [17], catalysis [18], adsorption [19], energy storage [20], drug delivery [21], and chemical sensing [22] because of their unique qualities, which include record-breaking surface areas, ultrahigh porosities, low density, high thermal stability, and tunable pore structures [23]. The two techniques that are now most frequently employed to recover MOFs from the reaction medium are filtration and centrifugation. MOFs can only be used on a limited scale due to their high cost, difficult separation methods, and relatively slow speed of separation. For this reason, creating a MOF material that is readily separated will be crucial to its eventual widespread use. To make their separation simple, the magnetization of MOF is the most applicable method.

Simple oscillation or agitation can be used to readily and uniformly spread magnetic nanoparticles (Fe_3O_4) in an aqueous or organic liquid phase. They may be directly separated from the liquid phase by applying an external magnetic field due to their high saturation magnetization, which eliminates the need for additional labor-intensive operating procedures like centrifugation and filtration [24]. These nanoparticles have the convenient ability to be reused. The applicability of Fe_3O_4 nanoparticles is limited due to the considerable particle aggregation that can occur from magnetic dipole interactions despite the comparatively straightforward production process. In order to compensate for this shortfall, cellulose nanocrystals [25], graphene [26], carbon nanotubes [27], and chitosan [28] have all been added to Fe_3O_4 nanoparticles.

Because of its special qualities, which include being affordable, renewable, degradable, plentiful, non-toxic, and ecologically benign, cellulose is a promising polymer for the creation of adsorbent compounds [29,30]. At the nanoscale, cellulose has a high aspect ratio and a large surface area, which makes adsorbent modification possible to attain superior adsorption [31,32]. Additionally desirable for the adsorbent reinforcement are nanocellulose's (NC's) extraordinary mechanical and chemical capabilities. The robustness and lifespan of adsorbents used in water treatment are further enhanced by these characteristics. These properties of NC allow their wide applications in adsorbents [33], flocculants [34], scaffolds [35], and drug carriers [36]. Our laboratory has utilized NC for the water treatment [37]. Also, many reported studies have combined NC and MOF. Using an *in situ* growing technique, Ma *et al.* created a ZIF-8@cellulose aerogel, which successfully adsorbed dyes and heavy metal ions [38]. Also, Wang *et al.* used UiO-66 on the cellulose aerogel [39] for adsorption applications. Zhu and colleagues blended cellulose aerogel with three distinct MOF materials (ZIF-8, UiO-66, and MIL-100(Fe)) to successfully adsorb heavy metals [40]. However, the high adsorption time and low adsorption capacity of these adsorbents need to be improved.

Herein, we aim to create a straightforward process for combining Fe_3O_4 nanoparticles, NC, and MOF to create a more powerful dye adsorbent (Fe_3O_4/NC/MOF) that is more effective. In this study, Zn(II)-based MOF was produced on a magnetic NC surface, and characterized *via* different techniques. It was then evaluated as an adsorbent to various anionic and cationic types of dyes (Congo red [CR], BB 54, BV 14, and AR 88) from water under a range of experimental parameters, including temperature, contact time, pH, initial dye concentration, and adsorbent dose. Also, a thorough analysis of isotherms, kinetics, thermodynamics, and equilibrium was conducted to evaluate the performance of this adsorbent with target dyes. The industrial application of this hybrid adsorbent appears highly promising due to its high adsorption capacity, effectiveness, and simple synthesis.

2 Materials and methods

2.1 Chemicals

Trisodium citrate ($Na_3C_6H_5O_7$), iron(II) sulfate heptahydrate ($FeSO_4{\cdot}7H_2O$), NC, benzene-1,3,5-tricarboxylic acid (BTC), zinc acetate dehydrate, 2,2,6,6-tetramethyl piperidine-1-oxyl (TEMPO), triethylamine (Et_3N), AR 88, BV 14, BB 54, and CR were supplied by Sigma-Aldrich. Sodium hydroxide (NaOH), nitric acid (HNO_3), sodium bromide (NaBr), sodium hypochlorite (NaClO), and *N*,*N*-dimethylformamide (DMF) were supplied by El-Gomhuria Co., Egypt. The analytical grade chemical raw materials listed above are all usable without additional purification. The distilled water used in all of the experiments was self-made.

2.2 Synthesis of Fe_3O_4 nanoparticles

A technique called reverse co-precipitation was used to create Fe_3O_4 nanoparticles. This technique was slightly modified from the literature [41]. First, 50 mL of deionized water was combined with 1 mL of $Na_3C_6H_5O_7$ (1 mM) and 50 mL of NaOH (1 M). After that, the mixture was vigorously stirred for 10 min at room temperature and 55.6 mg of $FeSO_4{\cdot}7H_2O$ was added. Black precipitates were seen when the salts were added to the alkaline solution, which may indicate that Fe_3O_4 nanoparticles were formed. After the solution was cooled to ambient temperature, the

precipitate was easily collected by a permanent magnet and microwave irradiated for up to 30 s. The black precipitates were air-dried overnight. After re-suspending in deionized water, the Fe_3O_4 nanoparticles were separated using a permanent magnet and centrifuged for 15 min at 6,000 rpm. After separating, the Fe_3O_4 nanoparticles were combined with 1 mL of deionized water to achieve a final concentration of 12 mg·mL^{-1}. This mixture was then kept at room temperature until used.

2.3 Synthesis of the Fe_3O_4/NC nanocomposite

Using a homogenizer, about 1 g of NC was distributed in distilled water. Next, 0.125 g of sodium bromide (NaBr) and 0.0125 g of TEMPO were added to the suspension of NC and stirred at room temperature. About 9.0 mL of sodium hypochlorite (NaClO) was added dropwise to the NC suspension to start the oxidation process. The suspension was supplemented with 0.5 M sodium hydroxide (NaOH) to keep the pH between 10 and 11 during the process. To halt the reaction, around 10 mL of ethanol was injected once the pH of the suspension reached a steady level. Ultimately, NC was thoroughly washed with distilled water and then freeze-dried. Subsequently, 50 mg of NC was mixed with 50 mL of deionized water, and 10 mL of Fe_3O_4 nanoparticles was added to the mixture and vigorously agitated for 2 h at room temperature. After creating the hybrid nanocomposite, they were separated using an external magnet and then re-dispersed for future use in 50 mL of deionized water.

2.4 Synthesis of zinc-based MOF (Zn-BTC)

A minor modification was made to the published process for synthesizing MOF [42]. DMF (25 mL) was used to dissolve BTC (0.53 g, 2.5 mmol) and Et_3N (2.7 mL). In addition, 0.72 g (3.3 mmol) of zinc acetate dihydrate was dissolved in the same volume of DMF. The two solutions were combined and swirled for 2.5 h. Centrifugation was used to recover the product, which was then cleaned thrice with DMF and twice with methanol. Ultimately, MOF was oven-dried at 70°C to get the desired dry product (0.9 g).

2.5 Synthesis of Fe_3O_4/NC/MOF nanocomposite

DMF (25 mL) was used to dissolve BTC (0.53 g, 2.5 mmol) and Et_3N (2.7 mL). Before adding 1 g of Fe_3O_4/NC, zinc acetate dihydrate (0.72 g, 3.3 mmol) was also dissolved in

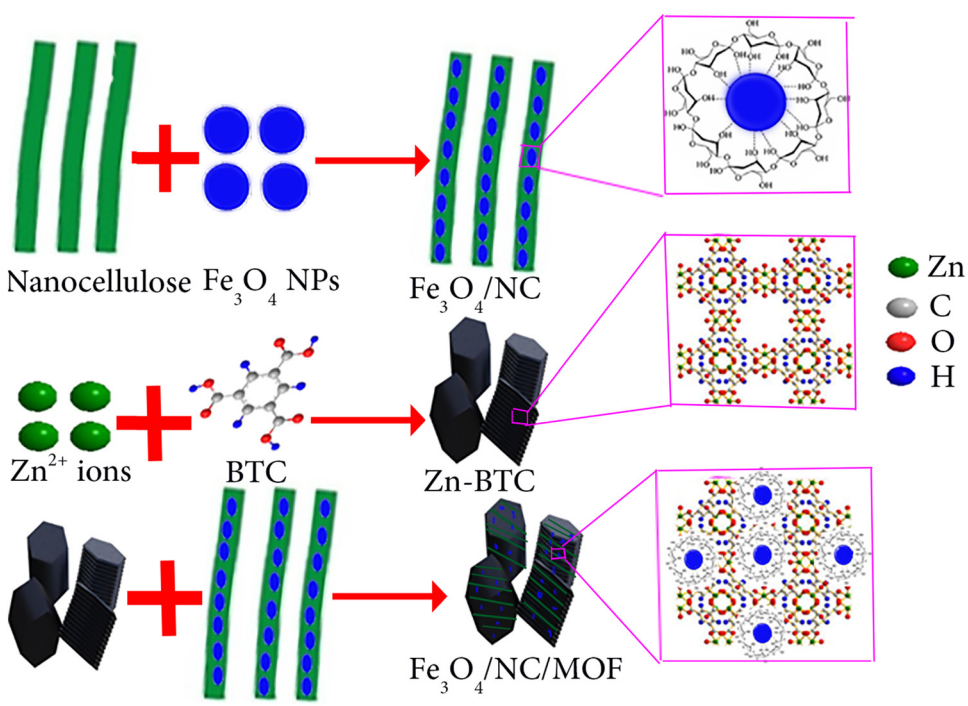

Scheme 1: Synthesis procedures and the structure of the as-prepared materials.

25 mL of DMF. These two solutions were combined and agitated mechanically for 30 min. The combined solution was then swirled for 2.5 h at room temperature. Following magnetic separation, the Fe_3O_4/NC/MOF nanocomposite was washed twice, alternatingly with DMF and methanol. Vacuum freeze-drying was then used to obtain the Fe_3O_4/NC/MOF nanocomposite. Scheme 1 illustrates the synthesis procedures and structure of the fabricated Fe_3O_4/NC/MOF nanocomposite.

2.6 Characterization of the as-prepared materials

Transmission electron microscopy (TEM) was performed using a JEOL JEM 2100 transmission electron microscope operating at 200 kV. The N_2 adsorption–desorption isotherms were measured at 77 K by the Brunauer–Emmett–Teller method using a Micromeritics ASAP 2020 M + C analyzer. The materials' surface morphology was investigated using a scanning electron microscope (SEM, S4800, Hitachi, Japan). X-ray diffraction (XRD) patterns of the produced materials were obtained using an X-ray diffractometer with Cu-K_α radiation (40 kV, 30 mA). With a scan step of 0.02°, the patterns were recorded in the 2θ region between 10° and 80°. Fourier-transform infrared (FTIR) spectra were recorded using a Perkin Elmer Spectrum 100 Fourier Transform Spectrometer. A vibrating sample magnetometer (VSM), a physical property measurement instrument, was used to measure the magnetic properties at 300 K as a function of the applied magnetic field, ranging from −80 to 80 kOe. X-ray photoelectron spectroscopy (XPS) (AXIS ULTRA DLD, Shimadzu, Japan) was performed to examine the materials' surface constituents.

2.7 Adsorption of organic dyes

The synthesized adsorbent was investigated for the removal of different organic dyes AR 88, BV 14, BB 54, and CR. The molecular structures of the four dyes are presented in Scheme 2. In the adsorption process, the ideal parameters and influencing variables for Fe_3O_4/NC/MOF dye removal were examined. Using 0.008 g as the adsorbent dose, the impacts of the initial dye concentration (0.001–0.8 g·L^{-1}) were examined for 20 min at pH = 2. Prior to mixing the dye solution with the adsorbent, 0.05 N hydrochloric acid or 0.05 N sodium hydroxide was added to the dye solution to correct the pH. The ideal amount of the adsorbent was found by mixing various quantities of the adsorbent (1 × 10^{-3} to 1 × 10^{-2} g) with 10.0 mL of polluted water for 20.0 min at 298 K, pH = 2–8, and an initial dye concentration of 20 mg·L^{-1} while stirring continuously at 500 rpm. The concentrations and adsorption of the dye solution were measured using a UV-Vis spectrophotometer. Subsequently, using the following equations, dye removal efficiency (%) and adsorption capacity at different time periods (q_e, mg·g^{-1}) were calculated:

$$q_e = (C_o - C_e/m)V, \quad (1)$$

$$\text{Efficiency}(\%) = (C_o - C_e)/C_o \times 100, \quad (2)$$

where C_e and C_0 (mg·L^{-1}) are the equilibrium concentration and initial concentration of the dye, respectively. The mass of the adsorbent was expressed as m (g), and V was the dye solution's volume. The dye concentration (0.01–0.8 g·L^{-1}) and adsorbent dose (1, 0.08, 0.06, 0.02, and 0.01 g·L^{-1}) were chosen for the investigations of adsorption isotherms and kinetics.

The recyclability of the synthesized Fe_3O_4/NC/MOF was investigated for the removal of organic dyes to determine

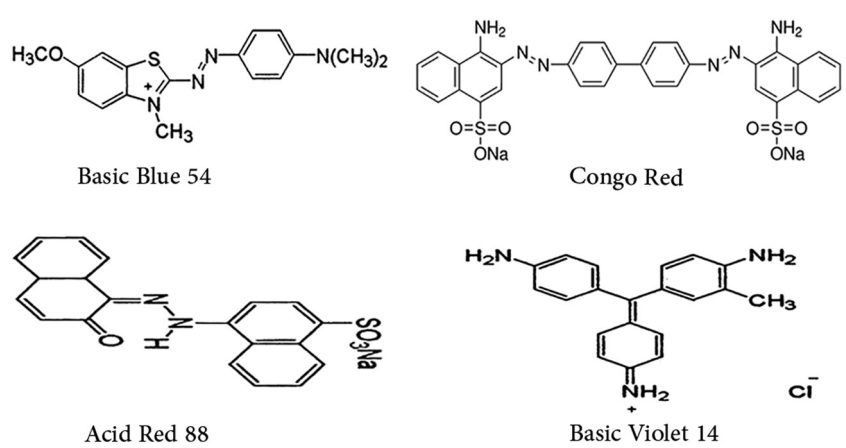

Scheme 2: The molecular structures of the four dyes used in the adsorption experiments.

its effectiveness as a reusable adsorbent. The reusability of Fe_3O_4/NC/MOF for dye adsorption was investigated under optimum conditions, which included an agitation rate of 500 rpm, a contact time of 20.0 min, pH of 2.0, a dosage of 0.08 g·L^{-1}, and a dye concentration of 20.0 mg·L^{-1}. The reusability study was investigated for up to four successive cycles. Each cycle consists of adsorption and desorption. In the adsorption part, the organic dyes were mixed with Fe_3O_4/NC/MOF under optimum conditions. After that, the adsorbent was collected using a magnet and reactivated. The reactivation process involved the desorption of adsorbed dyes from the surface of the adsorbent using a suitable eluent. Herein, the used eluent was ethanol 60% (10 mL) and NaOH 0.1 M (10 mL). After desorption, the adsorbent was washed using a mixed solvent of H_2O/EtOH and dried by heating under a vacuum at 55°C for 55 min to be ready for the next cycle. After each cycle, UV-Vis spectroscopy was employed to examine for any remaining dye residues.

3 Results and discussion

3.1 Characterization of materials

Figure 1a displays the XRD patterns for MOF and Fe_3O_4/NC/MOF. At 15.8°, a distinctive peak for NC was observed. This peak shows the normal diffraction pattern of type I cellulose and correlates with the (101) reflection [43]. Magnetic Fe_3O_4 nanoparticles have six unique peaks at 2θ = 57.2, 53.7, 43.2, 35.6, and 30.3°, as shown in Figure 1a [44,45]. After MOF was coated by the Fe_3O_4/NC nanocomposite surface, the pattern seen for Fe_3O_4/NC/MOF additionally included the peak characteristic for MOF at 11.0° [46], as shown in Figure 1a. These XRD findings verify that the composite product (Fe_3O_4/NC/MOF) retains both the magnetic nanoparticles and the MOF crystal structure. FTIR spectra were used to characterize the structures of the produced materials.

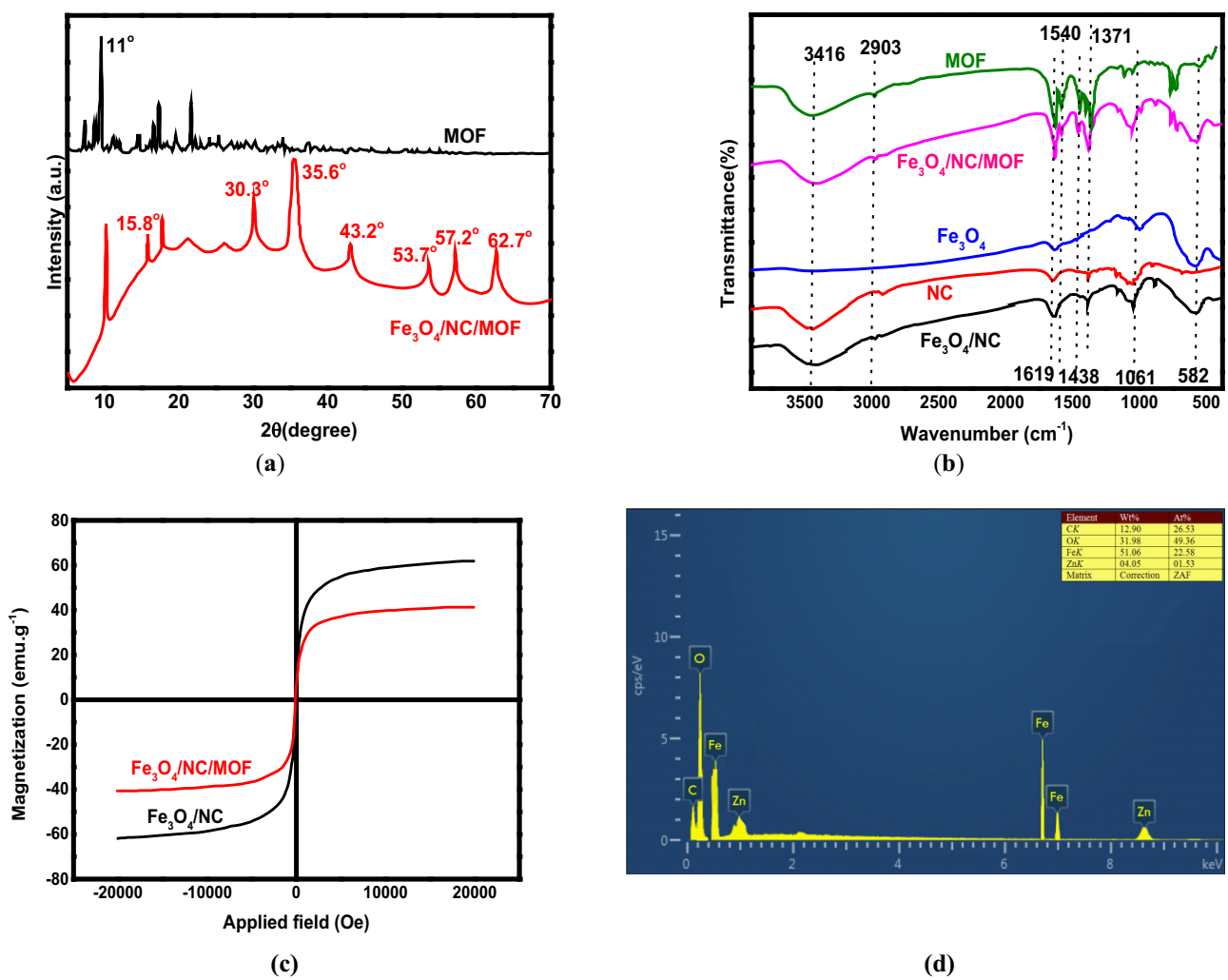

Figure 1: (a) XRD, (b) FTIR, (c) magnetization curves, and (d) EDX spectrum of the synthesized materials.

The MOF spectrum displays two peaks, corresponding to the asymmetric and symmetric carbonyl stretching vibrations of MOF, in the ranges of 1,619–1,540 and 1,438–1,371 cm^{-1} (Figure 1b) [47]. The Fe–O stretching vibration is represented by the peak at 582 cm^{-1} (Figure 1b) in the Fe_3O_4/NC nanocomposite spectrum, which is typical for Fe_3O_4 [48]. The 2,903 cm^{-1} band is associated with the C–H stretching vibration modes of NC, while the C–C bond vibrations are responsible for the bands at 1,161 and 1,064 cm^{-1} [49,50]. The vibration modes of O–H stretching are represented by the bands located at 3,416 cm^{-1} [51]. The FTIR spectrum of Fe_3O_4/NC/MOF also showed the typical peaks of MOF at 1,619–1,371 cm^{-1}, suggesting that MOF was successfully bonded to the Fe_3O_4/NC nanocomposite surface. The presence of hydroxyl groups in Fe_3O_4/NC/MOF was shown by the broad band at 3,416 cm^{-1} induced by the O–H stretching vibration. FTIR results indicated that carboxyl groups are abundant on the surfaces of Fe_3O_4 nanoparticles and NC, and MOF has a significant amount of them as well. Because the oxygen atoms of carboxylic and hydroxyl groups have free pairs of electrons, they can interact with the adsorbate molecules to produce complexes that are mediated by coordinative bonds.

The magnetic characteristics of Fe_3O_4/NC and Fe_3O_4/NC/MOF were examined using a VSM. The magnetic hysteresis loops acquired for these two magnetic materials are displayed in Figure 1c. The saturation magnetization of Fe_3O_4/NC was 62.70 emu·g^{-1}. This value dropped to 42.39 emu·g^{-1} with MOF loading. These findings suggest that the Fe_3O_4/NC/MOF can be quickly separated when a magnetic field is applied. After vigorous shaking, the Fe_3O_4/NC/MOF was separated by an external magnetic field in less than 40 s. Figure 1d presents the energy-dispersive X-ray spectra (EDX) distribution of C, O, Zn, and Fe in the Fe_3O_4/NC/MOF nanocomposite. The Fe/O ratio in the magnetic Fe_3O_4 nanoparticles (2.6) is higher than that in Fe_3O_4/NC/MOF (1.6), as shown in Figure 1d. This difference can be due to the increased oxygen concentration in MOF and NC, which suggests the production of Fe_3O_4/NC/MOF. Figure 2 displays the TEM images of NC, MOF, Fe_3O_4/NC, and Fe_3O_4/NC/MOF. Numerous hydroxyl (OH) groups on the NC surface (Figure 2a) can connect with one another through

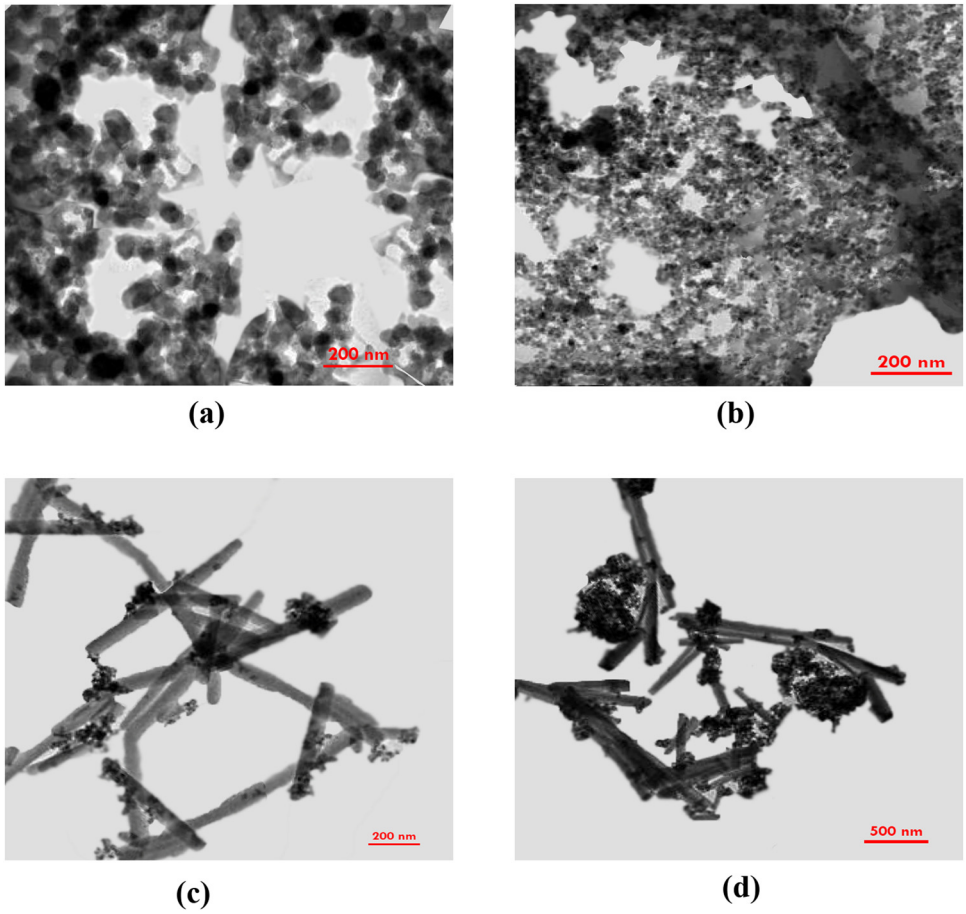

Figure 2: TEM images of (a) NC, (b) MOF, (c) Fe_3O_4/NC, and (d) Fe_3O_4/NC/MOF.

hydrogen bonding, which causes the cellulose rods to aggregate into spherical forms. Comparing the TEM image of NC (Figure 2a) with that of Fe_3O_4/NC (Figure 2c) in which NC was modified using magnetic nanoparticles, it is clear that the clustered NC has been distributed. The average length of the Zn-based MOF is shown in Figure 2b and d. It is also clear that Fe_3O_4/NC adhered to the surface of the prismatic MOF, indicating that the desired Fe_3O_4/NC/MOF was successfully fabricated.

Figure 3 displays the SEM images of NC, MOF, Fe_3O_4/NC, and Fe_3O_4/NC/MOF. According to Figure 3a, partially aggregated spherical particles were observed for the NC surface. Furthermore, not many triangular or quadrangular structures were seen on the NC surface. MOF crystals appear as flawless, prismatic pillar-like crystals in the SEM image (Figure 3b).

The surface of Fe_3O_4/NC showed irregularly shaped particles following treatment with the magnetic nanoparticles (Figure 3c). This discovery is explained by the interaction of the NC layer's surface with magnetic Fe_3O_4 nanoparticles. Eventually, following MOF coating by Fe_3O_4/NC, pillar-like crystals were seen on the composite surface (Figure 3d), proving the effectiveness of the coating process. Such MOF-based adsorbents have a large number of pores, and the low-temperature nitrogen adsorption method can be used to measure the pore size distribution, pore volume, and specific surface area of these materials. Figure 4a displays the isothermal adsorption/desorption isotherms of Fe_3O_4/NC, NC, and Fe_3O_4/NC/MOF determined at 77 K. Type IV of the IUPAC classification was consistent with the nitrogen adsorption/desorption isotherms of NC, and H1 type hysteresis loops were observed. This suggested that the NC samples have a mesoporous structure. The monomolecular layer adsorption process was completed when $P/P_0 < 0.1$, as indicated by the first inflection point of the N_2 adsorption–desorption isotherm of Fe_3O_4/NC/MOF. Further increase of the pressure causes the adsorption of the additional layer. There are an endless number of adsorption layers at the saturated vapor pressure. These are the type II isotherms for adsorption. Additionally, the specific surface area of Fe_3O_4/NC/MOF reached 66.3 $m^2 \cdot g^{-1}$, which might be attributable to the high specific surface area of MOF. In contrast, the BET-specific surface area of NC alone was 30.15 $m^2 \cdot g^{-1}$. This specific surface area of NC reached 40.45 $m^2 \cdot g^{-1}$ after the magnetization using Fe_3O_4 nanoparticles. The Barrett–Joyner–Halenda (BJH) technique yielded pore diameters of 3.85, 5.66, and 11.88 nm for Fe_3O_4/NC/MOF, Fe_3O_4/NC, and NC,

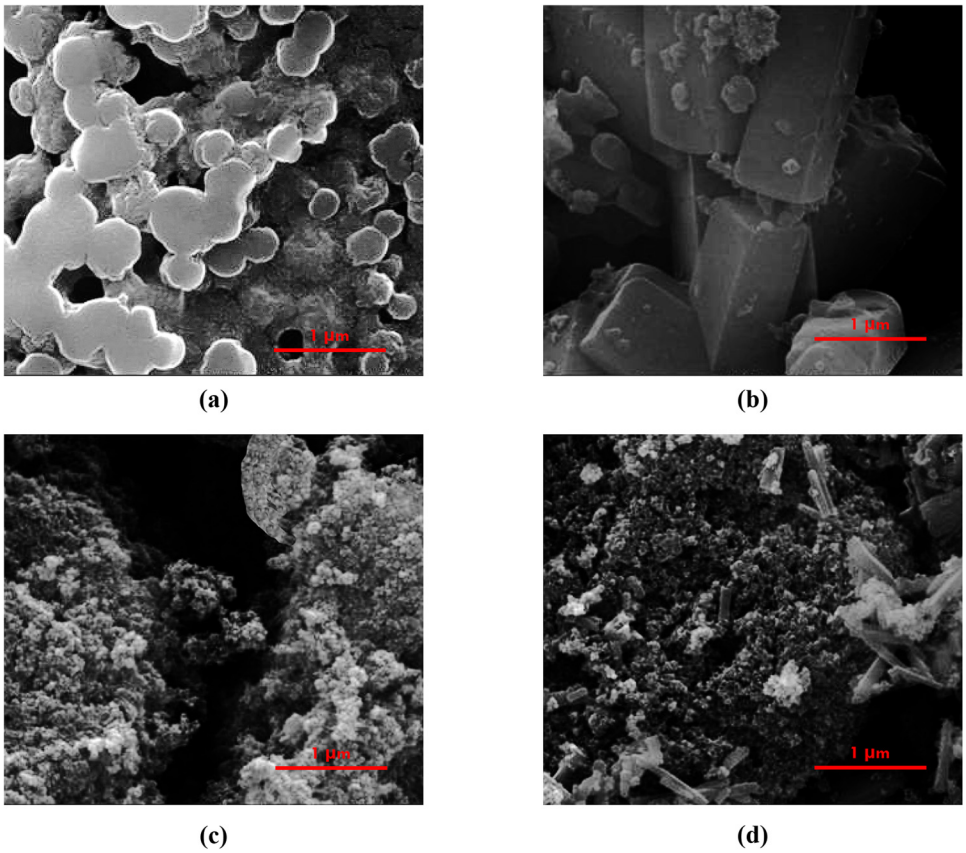

Figure 3: SEM images of (a) NC, (b) MOF, (c) Fe_3O_4/NC, and (d) Fe_3O_4/NC/MOF.

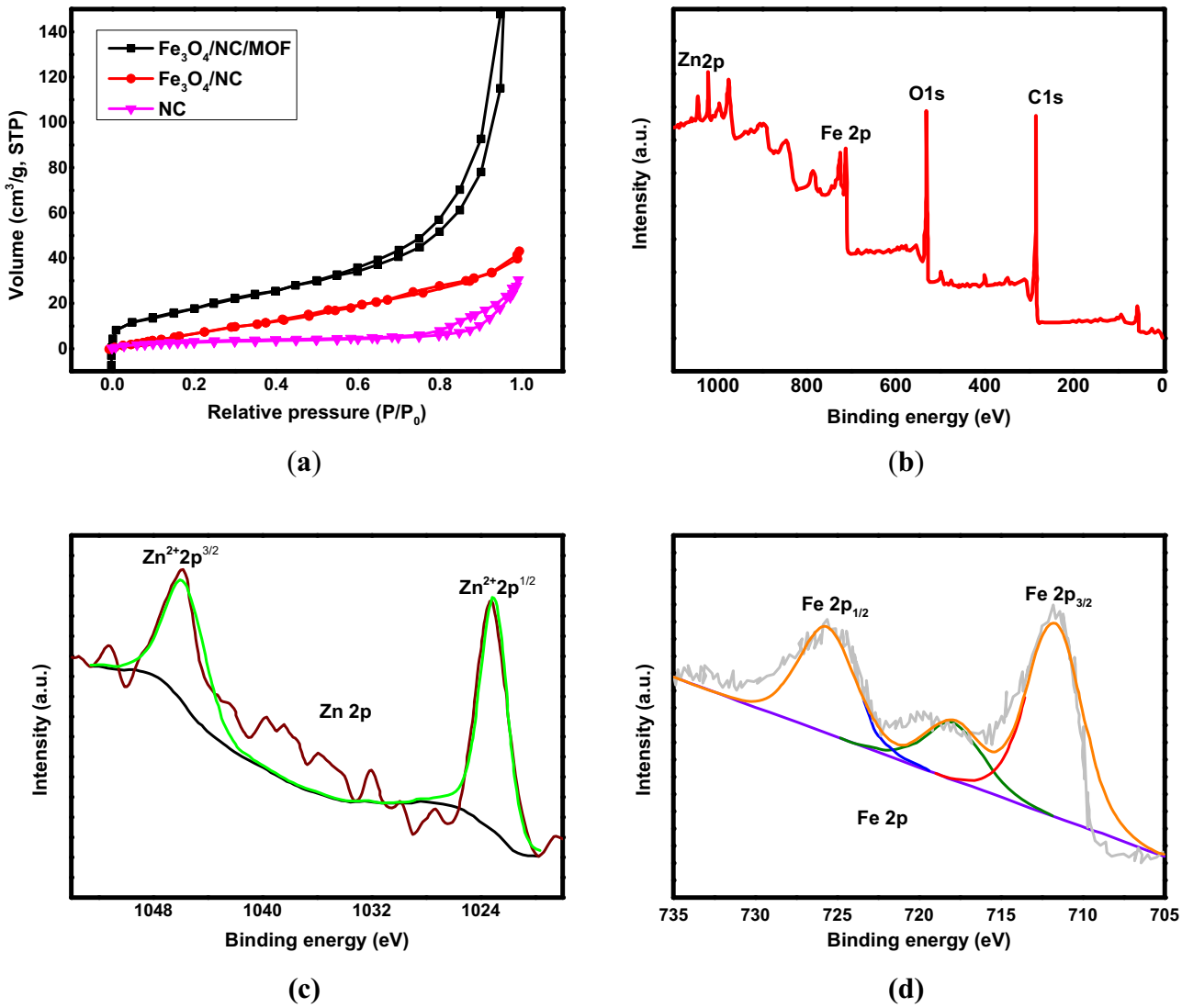

Figure 4: (a) N_2 adsorption–desorption isotherm, (b) XPS spectra full survey, (c) XPS spectra of Zn 2p, and (d) XPS spectra of Fe 2p of the synthesized materials.

respectively. The total pore volumes of Fe_3O_4/NC/MOF, Fe_3O_4/NC, and NC are 0.481, 0.067, and 0.813 $cm^2 \cdot g^{-1}$, respectively. The reason for this was that the pore diameter and pore volume significantly decreased as a result of MOF loading onto the NC's surface and internal channel blockage. To ascertain the oxidation states of the novel nanocomposite Fe_3O_4/NC/MOF and chemical bonding, an XPS spectrum was generated. The components Zn, C, O, and Fe are present in the Fe_3O_4/NC/MOF, according to the survey XPS spectrum shown in Figure 4b.

It was possible to demonstrate the oxidation states of zinc elements, Zn^{2+} $2p^{3/2}$ and Zn^{2+} $2p^{1/2}$, display significant peaks at 1,024 and 1046.55 eV, respectively, as shown in Figure 4c. The distinctive binding energies of Fe $2p^{3/2}$ (711.69 eV) and Fe $2p^{1/2}$ (725.42 eV) are responsible for the two peaks that make up the Fe 2p characteristic spectrum, as shown in Figure 4d. The XPS spectra results indicate the good incorporation between MOF and Fe_3O_4/NC in the nanocomposite confirming the successful fabrication of the desired adsorbent. We can conclude from the characterization results of XRD, FTIR, SEM, TEM, VSM, EDX, EBT, and XPS that the desired Fe_3O_4/NC/MOF nanocomposite was well constructed by the combination of MOF and the magnetic Fe_3O_4/NC nanocomposite.

3.2 Adsorption study

3.2.1 Optimization of adsorption parameters

First, the adsorption parameters for the removal of organic dyes CR, BB 54, BV 14, and AR 88 on the surface of the Fe_3O_4/

NC/MOF nanocomposite were optimized. These adsorption parameters were optimized through variations in pH, contact time, adsorbent dosage, initial dye concentration, and temperature. The resistance of dye molecules to transfer from the liquid phase to the solid phase ascertains the effect of initial dye concentration, a very important factor [52]. Therefore, an increase in the initial dye concentration would increase the adsorption efficiency. However, a dye molecule can move from bulk liquids to the adsorbent's external surface, suggesting that the concentration of dye molecules affects the amount of dye that is adsorbed onto the adsorbent [53]. As a result, the proportion of dye removed is higher at low initial concentrations and lower at high initial concentrations. The impact of dye concentration (ranging from 0.001 to 0.8 $g \cdot L^{-1}$) on removal capacity was examined in this study for 20.0 min at 298 K and 0.08 $g \cdot L^{-1}$ adsorbent dose. The Fe_3O_4/NC/MOF capacities of adsorption at equilibrium increase to 875.13, 877.71, 850.19, and 875.33 $mg \cdot g^{-1}$ from 13.0 $mg \cdot g^{-1}$ for AR 88, BB 54, BV 14, and CR, respectively; when the initial concentration of the organic dye is increased from 10 to 800 $mg \cdot L^{-1}$, as shown in Figure 5a.

The primary adsorption parameter that may be crucial to the adsorption process is temperature. Temperature has a significant impact on both the viscosity of the solution and the capacity of adsorption [54]. Consequently, determining the ideal temperature for the adsorption process is essential. To determine the effect of temperature on the Fe_3O_4/NC/MOF behavior, adsorption was examined at an initial concentration of dye equal to 20.0 $mg \cdot L^{-1}$ under

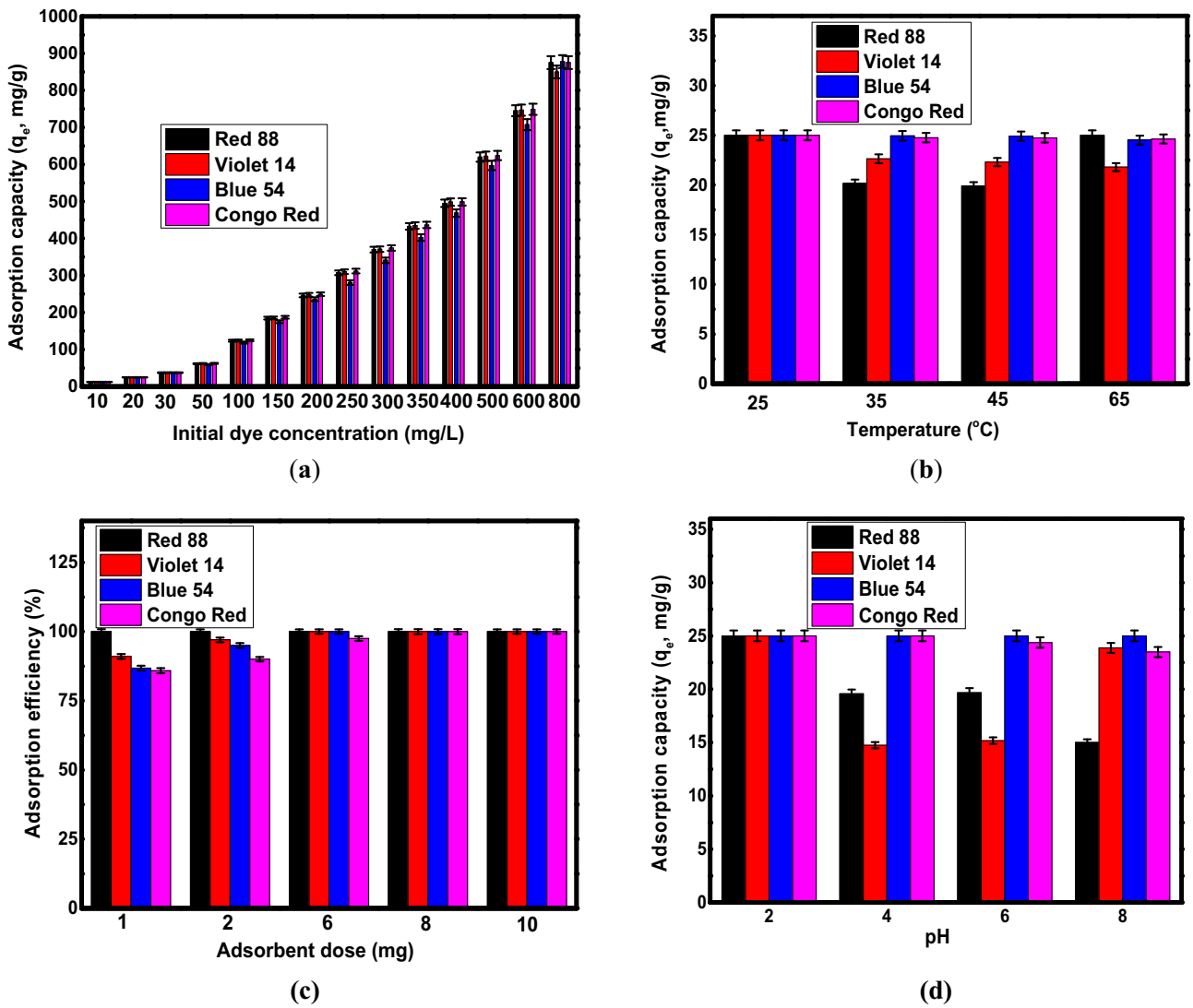

Figure 5: Effects of (a) initial dye concentration, (b) temperature, (c) adsorbent dose, and (d) pH for the removal of organic dyes using the Fe_3O_4/NC/MOF nanocomposite.

ideal conditions (stirring period: 20 min, initial dye concentrations: 20 mg·L^{-1}, pH = 2). The adsorption capacities for the removal of CR, BB (54), BV (14), and AR (88) are shown against temperature in Figure 5b, in the range of 25–65°C. It is clear that the removal of dyes was adversely affected by the increase of temperature. The ideal temperature for the Fe_3O_4/NC/MOF to remove dyes was 25°C. Since it shows the maximum adsorption ability for a given initial concentration of dye, the adsorbent dose is a crucial parameter [55]. Adsorption studies utilizing an adsorbent amount of 1.0–1,000 mg·L^{-1} at a temperature of 298 K, pH 2.0, and an initial concentration of dye of 20 mg·L^{-1} for a contact time of 20.0 min were used to establish the ideal quantity of Fe_3O_4/NC/MOF to adsorb dyes. Figure 5c demonstrates that when 0.001 g of Fe_3O_4/NC/MOF was employed as an initial dose, 85.76, 86.79, 90, and 100% of CR, BB 54, BV 14, and AR 88 were eliminated from their aqueous solutions. BB 54, BV 14, and AR 88 required dosages of 0.006, 0.006, and 0.001 g in that order; however, CR was found to be best removed by the Fe_3O_4/NC/MOF at a dosage of 8.0 mg. It was found that the elimination efficiency (%) of every dye increased and eventually reached 100% when the Fe_3O_4/NC/MOF dosage was increased by 8.0 mg. Thus, the dosage of 8.0 mg was chosen because increasing the adsorbent dose (quantity) further did not affect the dye treatment. Furthermore, the removal rate (%) of dyes is presented in Figure 5c, which increases when the amount of the adsorbent is increased until an equilibrium is reached. It may be clarified that an increase in the number of adsorption sites resulted in an increase in the specific surface area of the adsorbent and the availability of additional binding sites for the adsorption of dye [56]. This study found that the ideal adsorbent dose of Fe_3O_4/NC/MOF was 0.008 g, which resulted in a complete dye removal rate. pH is important in dye adsorption because it controls the surface charge of the adsorbent and the level of ionization of the adsorptive molecules [57,58]. At several pH values (ranging from 2.0 to 8.0), the effect of the starting solution pH on the dyes' ability to adsorb onto Fe_3O_4/NC/MOF was identified, with fixed values for the critical parameters (contact period of 20.0 min, dye concentration of 20 mg·L^{-1}, and adsorbent dose of 0.008 g/10.0 mL). Based on Figure 5d, all colors comprising CR, BB 54, BV 14, and AR 88 had their maximum adsorption capacity at pH = 2.0. The adsorption capacity of the anionic dye Acid red 88 diminishes as the pH of the solution increases from 2.0 to 8.0. The pH increase had no discernible effect on the adsorption capability of the other colorants. This could be caused by the numerous functional groups of the dyes as well as various interactions including dipole–dipole forces and hydrogen bonds between the adsorbate and the adsorbent. Under ideal conditions (initial concentration of dye = 20.0 mg·L^{-1}, 298 K, pH = 2.0, and adsorbent dose = 0.08 g·L^{-1}), the influence of contact time on the Fe_3O_4/NC/MOF adsorption capacity and dye removal percent was assessed. The investigation of the effect of contact time on adsorption behavior was determined in this study, and the removal efficiency was ascertained for model organic dyes as a function of contact time alternating from 10.0 to 60.0 min. The adsorption capacity as well as removal percentage of the Fe_3O_4/NC/MOF show a significant increase at first, and then increase at a relatively slow pace till equilibrium is achieved. After 20 min of the dye interaction with Fe_3O_4/NC/MOF, the most significant adsorption efficiency was achieved. This is attributed to the fact that a large number of empty surfaces are initially available for adsorption [59]. The remaining empty active sites are difficult and harder to find after a while. As a result, 20 min was chosen as the equilibrium contact time in this investigation.

3.2.2 Adsorption kinetics

The adsorption kinetics of Fe_3O_4/NC/MOF were examined in order to comprehend the reaction pathways of the adsorption process and the adsorption effectiveness of the adsorbents. The chemical and physical properties of the adsorbent serve as the basis for chemical kinetic models, whose evaluation is essential for revealing the variables influencing the rate of reaction [60]. Four kinetic models (*i.e.*, pseudo-first-order, pseudo-second-order, Elovich and intra-particle diffusion models) were used to study the adsorption kinetics of the Fe_3O_4/NC/MOF. The linear equations of the pseudo-first-order kinetic model [61] and the pseudo-second-order model [62] are shown in Eqs. (3) and (4), respectively:

$$\ln(q_e - q_t) = \ln q_e - K_1 t, \tag{3}$$

$$\frac{t}{q_t} = \frac{1}{K_2 q_e^2} + \frac{1}{q_e} t, \tag{4}$$

where k_1 and k_2 are the rate constants for the pseudo-first-order (min^{-1}) and pseudo-second-order adsorption kinetics (g·mg^{-1}·min^{-1}), respectively; q_t (mg·g^{-1}) and q_e (mg·g^{-1}) are the adsorption capacities at the reaction time t (min) and at equilibrium, respectively. The pseudo-first-order kinetic model sufficiency is represented by a straight line in the plot of $\ln(q_e - q_t)$ against t (Figure 6a), which shows a relationship between the intercept and slope. It is possible to ascertain the model parameters (k_1 and predicted q_e). The compatibility of pseudo-second-order kinetics on the dye removal at different adsorbent doses from single systems was examined using a linear graph of t/q_t against t. The slope of the t/q_t against t plot (Figure 6b) yields the value of q_e, and the initial adsorption rate value yields K_2.

Eq. (5) represents the Elovich equation, which is another kinetic model equation related to the adsorption capacity [63]:

$$q_t = \frac{1}{\beta}\ln(\alpha\beta) + \ln(t). \quad (5)$$

The Elovich constants α and β denote the initial adsorption rate ($g{\cdot}mg^{-1}{\cdot}min^{-1}$) and the desorption constant ($mg{\cdot}g^{-1}{\cdot}min^{-1}$), respectively. The plot of q_t against ln t (Figure 6c) is used to determine the Elovich constants.

The adsorption mechanism was further examined using the kinetic intra-particle diffusion model (Eq. (6)) [64]. The linear form is displayed as follows:

$$q_t = k_{id}t^{0.5} + c, \quad (6)$$

where c is the thickness of the boundary layer ($mg{\cdot}g^{-1}$), k_{id} is the rate constants for the intra-particle diffusion rate constants ($mg{\cdot}g^{-1}{\cdot}h^{-0.5}$), and q_t ($mg{\cdot}g^{-1}$) is the adsorption capacity at the reaction time t (min). By plotting linearly q_t versus $t^{0.5}$ (Figure 6d), the intra-particle diffusion kinetics constants (c and K_{id}) were obtained. Table 1 displays the kinetic constants of the as-mentioned four models. The adsorption process, according to the results, more closely matched the pseudo-second-order model. In this model, Table 1 displays the linear plot with the highest correlation coefficients.

The pseudo-first-order postulates that a single mechanism or process working on a single class of adsorbing sites is the only one capable of limiting the absorption rate. Table 1 and Figure 6a indicate that compared to the experimental data,

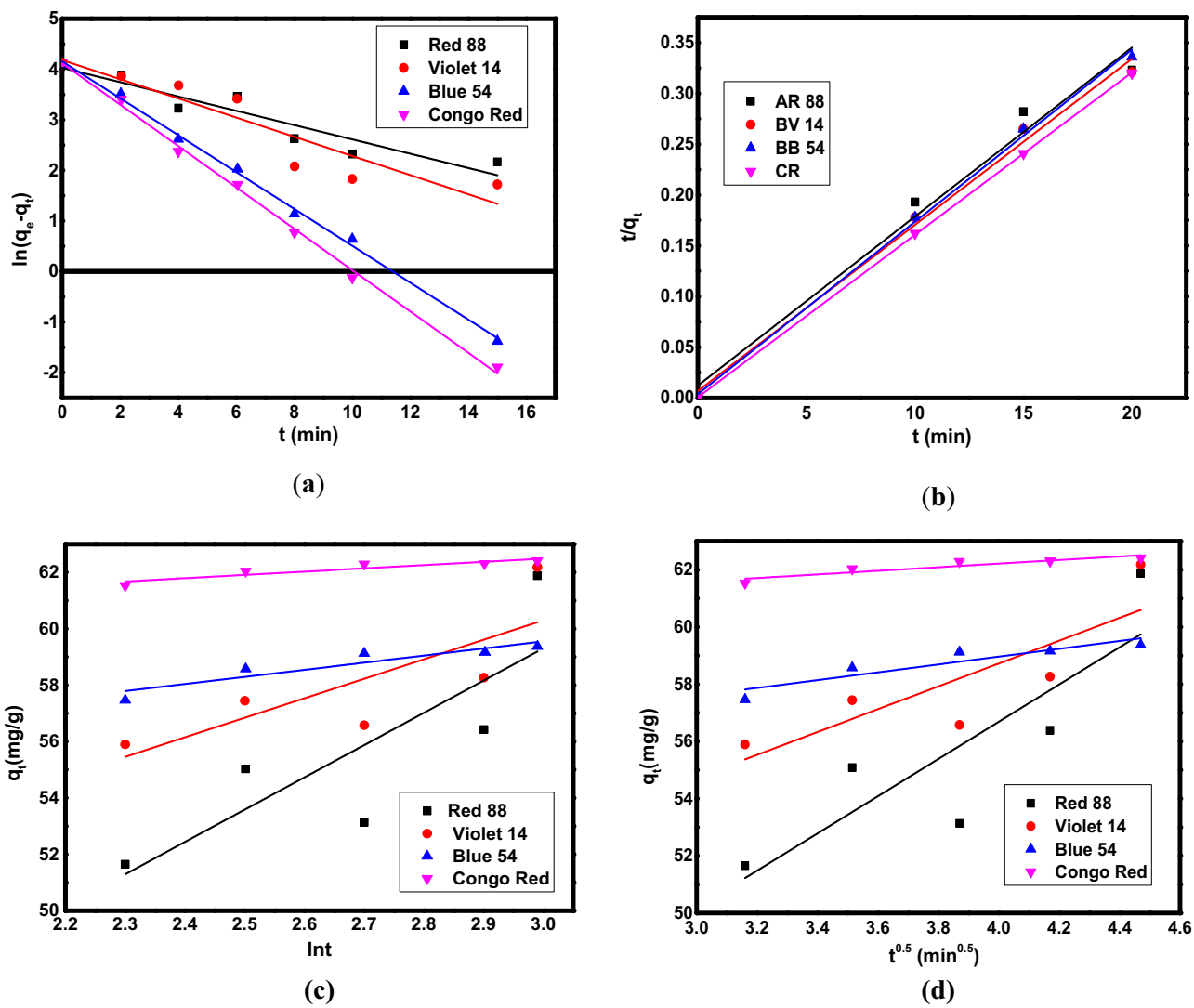

Figure 6: The fitting of experimental adsorption data to (a) pseudo-first-order, (b) pseudo-second-order, (c) Elovich, and (d) intra-particle diffusion kinetic models.

Table 1: Kinetic parameters for the adsorption of different dyes on the surface of the Fe_3O_4/NC/MOF nanocomposite

Model	Parameter Initial concentration (mg·L^{-1})	CR 50	BB 54 50	BV 14 50	AR 88 50
Pseudo-first-order	$q_{e,exp}$ (mg·g^{-1})	63.30	60.29	63.05	62.79
	$q_{e,cal}$ (mg·g^{-1})	60.07	62.88	54.32	56.55
	K_1 (min^{-1})	0.4167	0.3505	0.1699	0.1380
	R^2	0.9976	0.9979	0.9201	0.9445
Intra-particle diffusion	K_{id} (g·min^{-1}·mg^{-1})	0.6798	1.5678	4.5889	7.5244
	C (mg·g^{-1})	59.50	52.89	40.29	26.31
	R^2	0.8975	0.8798	0.7778	0.7999
Pseudo-second-order	$q_{e,cal}$ (mg·g^{-1})	63.40	59.76	61.88	60.99
	K_2(g·min^{-1}·mg^{-1})	0.3657	0.0741	0.0389	0.0330
	R^2	1.0	0.9980	0.9931	0.9880
Elovich model	β (g·mg^{-1})	0.759	0.349	0.120	0.080
	α (mg·g^{-1}·min^{-1})	3.13456941	169642386.813	508.284	50.632
	R^2	0.9129	0.9116	0.7446	0.7943

pseudo-first-order did not accurately compute the adsorption capacities for the manufactured material. Furthermore, the R^2 values deviate slightly from linearity. Because several sorption sites and mass transfer may be incorporated into the process mechanism, this model is therefore not suited to fully characterize the sorption processes onto heterogeneous surfaces. In comparison to the other three kinetic models, the adsorption processes more closely matched the pseudo-second-order reaction kinetic model when taking into account the coefficient of the determinant . The best fitting model for the higher correlation coefficients of CR, BB 54, BV 14, and AR 88 (R^2 = 1.0, 0.9980, 0.9931, and 0.9880) for the adsorption of dyes on Fe_3O_4/NC/MOF is the pseudo-second order model, as shown in Table 1. It appears from this that the adsorption mechanism is more similar to chemisorption. However, with R^2 better than 0.99, it is evident that the pseudo-first-order and pseudo-second-order models both fit the experimental data well of CR and BB 54 dyes. Based on these findings, we may conclude that the CR and BB 54 adsorption process onto Fe_3O_4/NC/MOF can be described by both pseudo-first-order and pseudo-second-order models. The adsorption of dye molecules to the surface of the solid adsorbent and enabling them to enter the pores is the slower step in the usually multi-step process of adsorption. So, the diffusion step is very important in the adsorption process. However, the diffusion mechanism is not identified by the first- and second-order kinetic models. Therefore, it is important to assess the experimental data using the intra-particle diffusion model (Eq. (6)). The intra-particle diffusion model suggested that the adsorption processes of dye molecules could occur *via* several steps [65]. These steps include the transport of the dyes in the bulk solution, film diffusion of these dyes at the boundary layer of the adsorbent, diffusion of dye molecules from the bulk solution to the external surface of the adsorbent material, and diffusion through small pores of the adsorbent. These steps are followed by the chemical binding of dyes with the adsorption sites. Finally, the equilibrium of adsorption was achieved and the maximum adsorption was obtained. Subsequently, based on the findings of the kinetic modeling, it was shown that surface chemisorptions that took place at the boundary layers of the developed material controlled the adsorption of dyes from the contaminated water onto the prepared MOF-based adsorbent.

3.2.3 Adsorption isotherm

Adsorption isotherms can reflect the surface characteristics of the adsorbent at the micro level. This is based on the interaction of the adsorbent with adsorbate molecules. This interaction determines the homogeneity or heterogeneity of the solid surface of the adsorbent and the type of coverage between the adsorbent and adsorbate. So, the isotherms of adsorption are important mathematical models to find the appropriate model that can be used for design purposes [66]. Adsorption isotherms also provide certain physicochemical details about how the adsorption takes place and how the reaction between the adsorbate and adsorbent surface occurs [67]. The equilibrium of dyes adsorbed by Fe_3O_4/NC/MOF was described in this work using the Freundlich, Langmuir, and Temkin isotherms. The adsorption data were fitted using the Freundlich model (Eq. (7)), Langmuir model (Eq. (8)), and Temkin model (Eq. (10)) as indicated in the following [68–70]:

$$\ln q_e = \ln K_F + \frac{1}{n}\ln C_e, \tag{7}$$

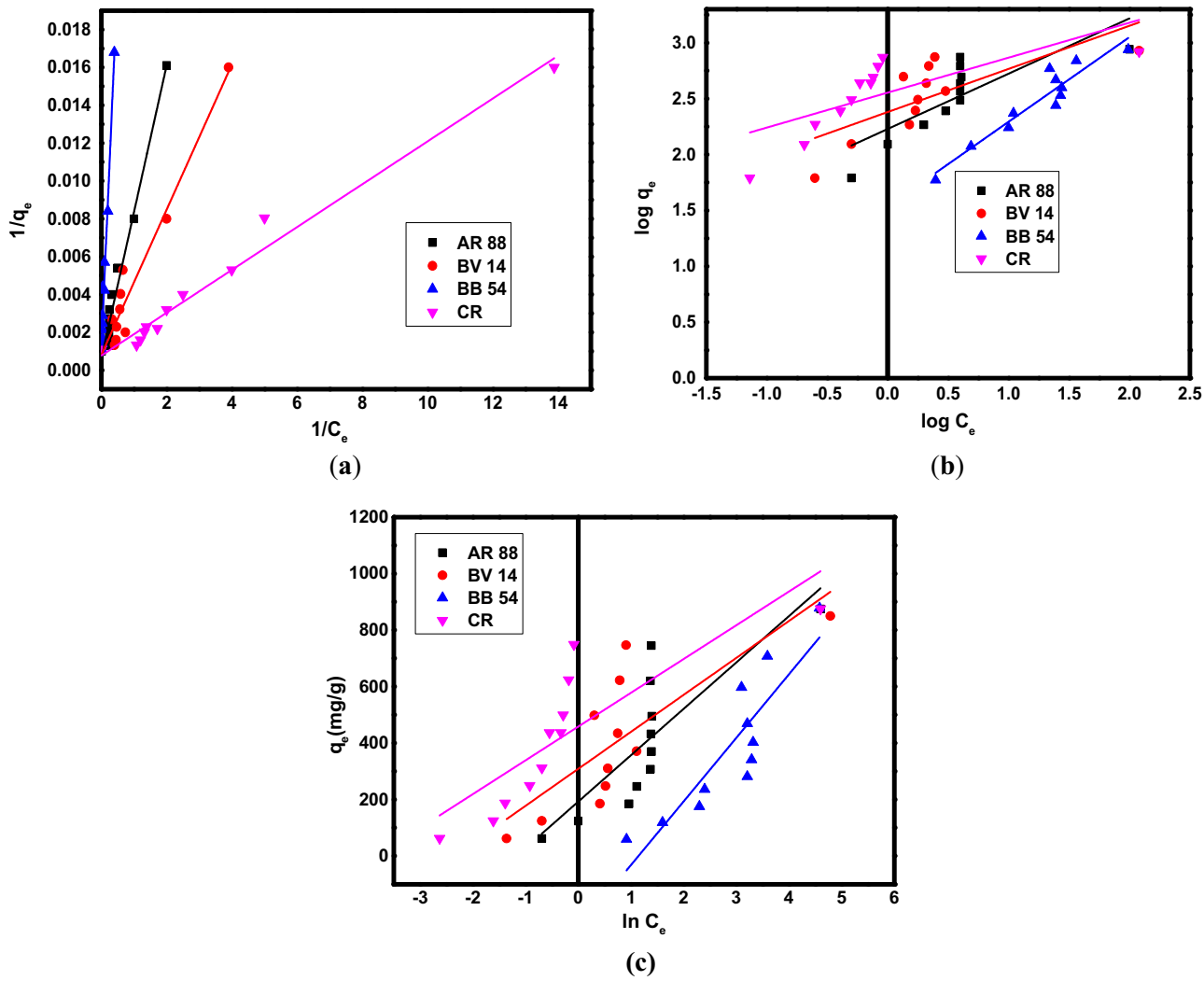

Figure 7: The fitting of experimental data to (a) Langmuir, (b) Freundlich, and (c) Temkin isotherm models for the adsorption of organic dyes on Fe_3O_4/NC/MOF.

$$\frac{C_e}{q_e} = \frac{C_e}{q_m} + \frac{1}{K_l q_m}, \tag{8}$$

$$R_L = \frac{1}{(1 + K_l C_o)}, \tag{9}$$

$$q_e = \frac{RT}{b_T} \ln K_T + \frac{RT}{b_T} \ln C_e, \tag{10}$$

where the adsorption intensity and adsorption capacity per unit concentration are related to the Freundlich constants $1/n$ and K_F, respectively. The maximal adsorption capacity is denoted by q_m (mg·g^{-1}), and the Langmuir constant for the adsorbent and adsorbate requirements is described by (K_L) (L·mg^{-1}). K_T is the equilibrium binding constant related to the first energy (L·g^{-1}), and b_T is the Temkin constant, which denotes the sorption point (kJ·mol^{-1}). R_L denotes the dimensionless separation constant and C_o denotes the initial concentration of the dye. According to the Langmuir model, there is no adsorbent transmission through the surface; instead, adsorption takes place within homogeneous locations over the absorbent [71]. However, the reversible, monolayer, non-ideal adsorption that is necessary for the Freundlich isotherm model may be familiar with multiple-layer adsorption on heterogeneous surfaces with different affinities and adsorption energies [72]. According to the Temkin isotherm model, the adsorption heat decreased linearly as the absorbent surface's coverage increased [73]. A consistent distribution of the binding energy is among the characteristics of this model. By plotting $1/C_e$ against $1/q_e$ linearly, the isotherm constants (q_m and K_L) in the Langmuir model were determined, as shown in Figure 7a. The Freundlich isotherm constants of dye removal were examined using a linear plot of log C_e against log q_e, as shown in Figure 7b. The Temkin isotherm was examined using the linear

Table 2: Isotherm parameters for the removal of organic dyes on the Fe_3O_4/NC/MOF surface

Model	Parameters	CR	BB 54	BV 14	AR 88
Freundlich model	n	3.05	1.35	2.61	2.04
	K_f (mg·g^{-1})	364.21	34.36	240.34	169.33
	R^2	0.5590	0.9015	0.5478	0.6469
Langmuir model	K_L (L·mg^{-1})	0.730	0.030	0.209	0.080
	q_m (mg·g^{-1})	1249	999.0	1249	1667.55
	R^2	0.9790	0.9700	0.950	0.9750
Temkin model	b_T (J·mol^{-1})	20.69	11.00	18.89	17.10
	K_T (L·mg^{-1})	46.20	3.15	10.60	3.30
	R^2	0.6989	0.7810	0.6160	0.6720
Separation factor (R_L)	C_0 (mg·L^{-1})	0.027–0.002	0.445–0.048	0.088–0.006	0.207–0.016

plot of C_e against q_e, as shown in Figure 7c, which is compatible with the dye adsorption data obtained using Fe_3O_4/NC/MOF. The isotherm constants of the three models are summarized in Table 2.

According to Table 2, it is suggested that the adsorption isotherm data can be satisfactorily provided by the Langmuir model. The Langmuir adsorption isotherm was the most appropriate model of all. According to the correlation coefficients (R^2) of the isotherm models, the Langmuir isotherm has the highest correlation, indicating dye adsorption on a homogenous surface. The essential characteristics of the Langmuir isotherm model are expressed by the equilibrium parameter (R_L) or dimensionless separation constant. The value of R_L indicates whether the isotherm is favorable ($0 < R_L < 1$), irreversible ($R_L = 0$), linear ($R_L = 1$), or unfavorable ($R_L > 1$). Table 1 shows that all of the R_L values were between 0 and 1, indicating that Fe_3O_4/NC/MOF adsorbed the dyes in a favorable manner. According to the Langmuir model, the highest monolayer adsorption capacities (q_m) for the removal of CR, BB 54, BV 14, and AR 88, were 1,249, 999.0, 1,249, and 1667.55 mg·g^{-1}, in that order. For comparison, the adsorption capacity of Fe_3O_4/NC/MOF was compared with that of the previously reported adsorbents, as listed in Table 3. The adsorption capacity of Fe_3O_4/NC/MOF

Table 3: Comparison of the removal capacity of previously reported adsorbents with Fe_3O_4/NC/MOF for adsorption of organic dyes

Adsorbent	Pollutant	Adsorption capacity (q_m, mg·g^{-1})	Ref.
Fly ash	CR	22.12	[74]
Zeolite	CR	9.23	[75]
Padina gymnospora	CR	12.38	[75]
Zeolite/algae composite	CR	12.25	[75]
Physically activated bottom ash	CR	106.61	[76]
Ni/Co-LDH	CR	909.2	[77]
Ni/Zn MOF	CR	460.90	[78]
MOF-5/Cu	CR	357.42	[79]
Fe_3O_4/NC/MOF	CR	1248	This study
Theobroma cacao shells	BV 14	980.39	[80]
Calophyllum inophyllum shells	BV 14	1416.43	[80]
Curcuma angustifolia scales	BV 14	208.33	[81]
Bottom ash	BV 14	6.39	[82]
Fe_3O_4/NC/MOF	BV 14	1248.3	This study
MNZnFe	AR 88	111.0	[83]
Alunite	AR 88	21.0	[84]
Anion membrane	AR 88	42.0	[85]
Activated carbon	AR 88	109.0	[86]
Fe_3O_4/NC/MOF	AR 88	1665.89	This study
Sodium alginate (SA)	BB 54	254.0	[87]
Na^+-rectorite (Na^+-REC)	BB 54	237.0	[87]
SA/Na^+ REC	BB 54	388.0	[87]
Fe_3O_4/NC/MOF	BB 54	999.88	This study

was more significant (Table 3) than that in the majority of the other adsorbents' reported values. The unique structure of Fe_3O_4/NC/MOF is responsible for its exceptional adsorption capabilities. This may be attributed to a large number of adsorption sites on its surface with large heterogeneity and diversity, which are energetically identical to provide homogeneous adsorption. That is, it offers organic framework adsorption sites in addition to Zn adsorption sites in addition to the active sites present on the surface of NC. Also, the ligands of MOF exhibit a π–π interaction with organic dyes because of their aromatic rings. Fe_3O_4/NC/MOF was discovered to have a significantly larger surface area than MOF alone that had just clumped together. The porous structure, their large specific extent, and more active adsorption sites are other factors that contribute to this adsorbent's increased adsorption capacity. The Fe_3O_4/NC/MOF has been found to have a comparatively higher adsorption capacity, indicating its viability and suitability as an inexpensive, practical, and efficient adsorbent in the adsorption process to remove dyes. Scheme 3 illustrates the adsorption sites of the prepared Fe_3O_4/NC/MOF in which different sites participated in dye removal with a variety of interactions.

3.2.4 Thermodynamic parameters of adsorption

Experiments were conducted between 25 and 65°C to investigate the adsorption thermodynamics during the dye adsorption by the Fe_3O_4/NC/MOF nanocomposite. The orientation and viability of the Fe_3O_4/NC/MOF nanocomposite for dye adsorption were assessed using thermodynamic parameters. The following equations were used to calculate the thermodynamic parameters such as the change in the Gibbs free energy (ΔG, kJ·mol^{-1}), enthalpy (ΔH, kJ·mol^{-1}), and entropy (ΔS, J·mol^{-1}·K^{-1}):

$$\Delta G = -\mathrm{RT}\ln K_\mathrm{d}, \tag{10}$$

$$\Delta G = \Delta H^\circ - T\Delta S^\circ, \tag{11}$$

$$\ln K_\mathrm{d} = \frac{\Delta S^\circ}{R} - \frac{\Delta H^\circ}{\mathrm{RT}}. \tag{12}$$

Plotting $\ln(q_e/c_e)$ versus q_e yields the sorption equilibrium constant, K_d. R is the ideal gas constant (=8.314 J·mol^{-1}·K^{-1}). The linear plot of $\ln K_d$ against $1/T$ (Van't Hof plot) was used to investigate the values of ΔH and ΔS using the slope and intercept, as shown in Figure 8a. The thermodynamic

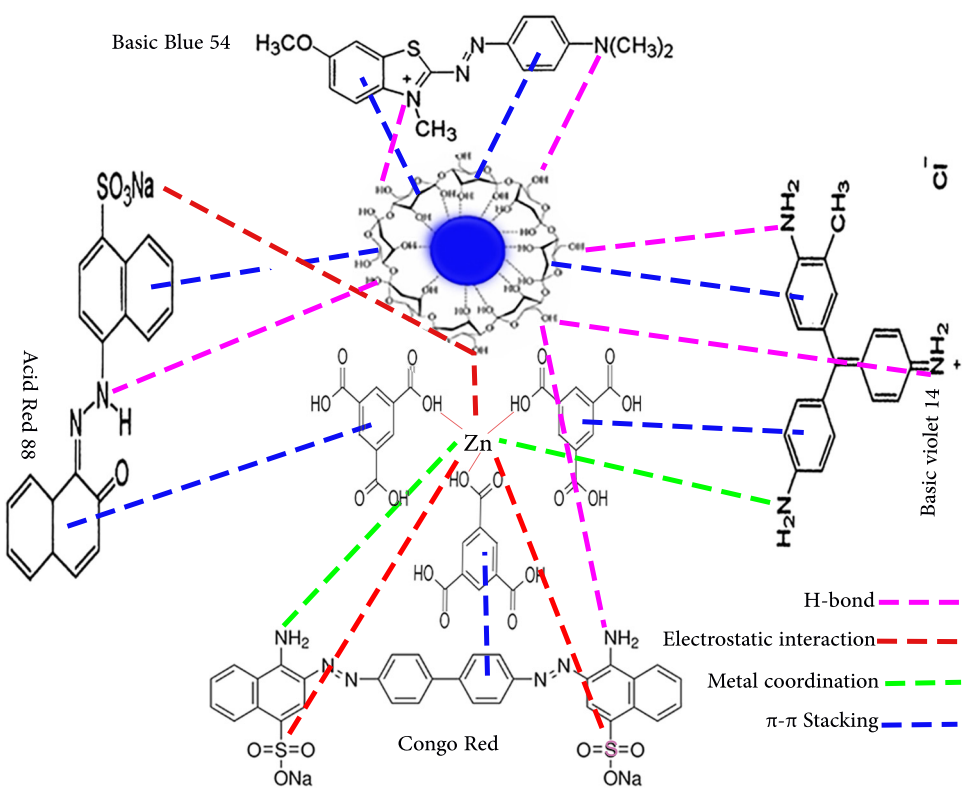

Scheme 3: Suggested adsorption mechanism of the Fe_3O_4/NC/MOF nanocomposite towards organic dyes.

parameters of adsorption are presented in Table 4. For all dyes, the spontaneous adsorption process is represented by the negative values of Gibb's free energy, ΔG [88]. During the adsorption process, a decrease in randomness at the solid-solution interface is indicated by a negative value of entropy (ΔS) [89].

The process involved increasing the temperature to enhance the mobility of the dye molecules, allowing them to move from the solid to the liquid phase. Furthermore, the exothermic adsorption of BV 14, BB 54, and CR onto Fe_3O_4/NC/MOF is shown by the negative value of enthalpy (ΔH) [90]. The adsorption process of AR 88 demonstrated endothermic qualities, as demonstrated by the positive value of ΔH [91]. On the other hand, as indicated by the positive value of ΔS, randomness increased at the solid-solution interface [92].

3.2.5 Reusability of Fe_3O_4/NC/MOF for dye adsorption

For commercial applications, the reusability of adsorbents is also a critical metric for assessing adsorption performance [93]. This contributes significantly to the decrease in the material cost of water treatment [94]. Adsorption–desorption tests were carried out in this work to investigate the adsorbent's regeneration. The adsorption of dyes from water by Fe_3O_4/NC/MOF has good regeneration performance and stability even after 4 cycles, as seen in Figure 8b. It should be mentioned that the elimination percentage was still higher than 80% after three cycles. Conversely, the Fe_3O_4/NC/MOF's regeneration rate of organic dyes decreased and lost its initial adsorption efficiency. This decrease shows that Fe_3O_4/NC/MOF has a high affinity toward organic dyes. This could be explained by the fact that the dye molecules can form very strong bonds with the functional groups on the surface of Fe_3O_4/NC/MOF. Also, the eluent could not totally desorb some of the dye-occupied active sites on the surface of Fe_3O_4/NC/MOF. However, the removal efficiency was still acceptable after the third cycle. Therefore, this adsorbent may be thought of as an effective and recyclable dye elimination option.

3.2.6 Application of Fe_3O_4/NC/MOF for wastewater sample

Further testing of the adsorption capabilities of Fe_3O_4/NC/MOF towards organic dyes in model wastewater (textile sample) was done to assess the technology's potential for use in real-world applications. A membrane filter with a 0.45-mm pore size was used to filter the wastewater sample in order to eliminate the suspended particle debris. As a real sample, one solution with 50.0 mg·L^{-1} of CR in wastewater was made. Then, 0.016 g of the adsorbent was added to 100.0 mL of wastewater at pH = 2. The blended solution was shaken for 20 min. The starting and final concentrations of the target species were found using the conventional addition method, which was used to conduct the assays. Different volumetric flasks were filled with 20.0 mL of wastewater samples each in order to achieve this goal. To achieve different concentrations of the CR dye, the standard CR solutions were then added in various proportions (0, 0.25, 0.5, and 0.75 mL of 1,000 mg·L^{-1}), and the solutions in the flasks were well mixed and diluted to an appropriate level. The UV-Vis spectrophotometry

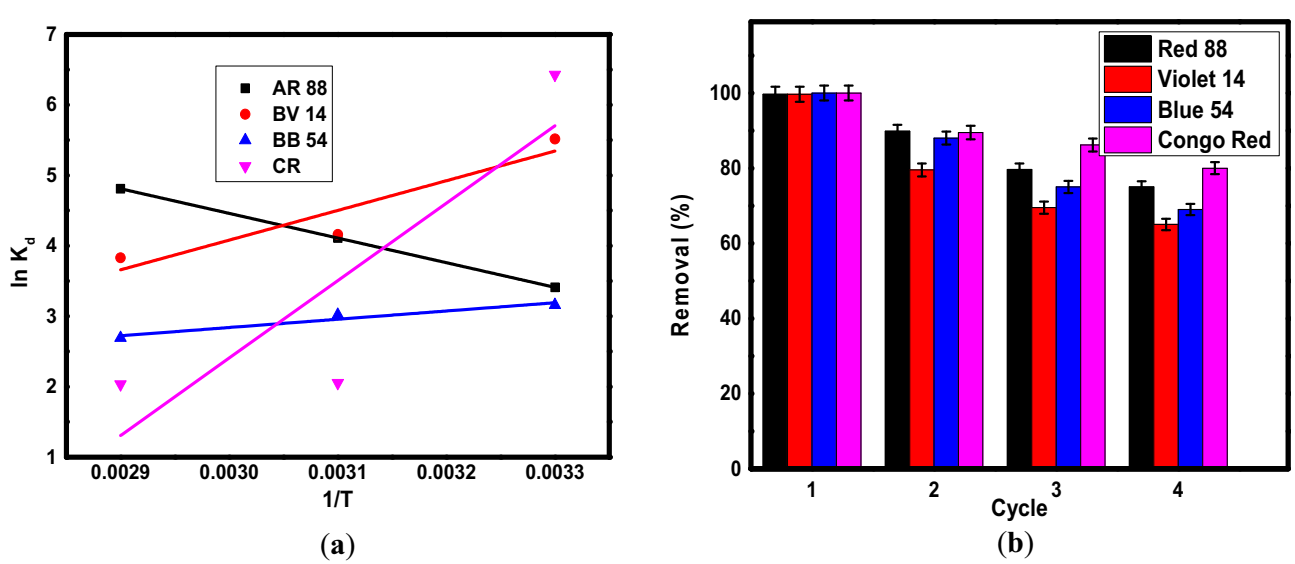

Figure 8: Van't Hof plot (a) and reusability (b) for the adsorption of organic dyes on the surface of Fe_3O_4/NC/MOF.

Table 4: Thermodynamic parameters for the adsorption of dyes on the surface of Fe_3O_4/NC/MOF

Temperature (K)	**CR**			**BB 54**			**BV 14**			**AR 88**		
	$\Delta G°$ (kJ·mol^{-1})	**$\Delta H°$ (kJ·mol^{-1})**	**$\Delta S°$ (J·mol^{-1}·K^{-1})**	**$\Delta G°$ (kJ·mol^{-1})**	**$\Delta H°$ (kJ·mol^{-1})**	**$\Delta S°$ (J·mol^{-1}·K^{-1})**	**$\Delta G°$ (kJ·mol^{-1})**	**$\Delta H°$ (kJ·mol^{-1})**	**$\Delta S°$ (J·mol^{-1}·K^{-1})**	**$\Delta G°$ (kJ·mol^{-1})**	**$\Delta H°$ (kJ·mol^{-1})**	**$\Delta S°$ (J·mol^{-1}·K^{-1})**
298.18	−15.95	−91.32	−253.94	−7.84	−9.76	−5.65	−13.67	−35.04	−71.20	−8.46	29.10	124.33
313.18	−5.43			−8.00			−11.00			−10.88		
338.18	5.73			−7.57			−10.77			−13.53		

method was used to calculate the dye concentrations in the solution. Then, the concentration of dyes was plotted against the absorption to get a standard calibration curve. This curve was used to find the unknown concentration of the dye. The UV spectra of CR wastewater samples before and after adsorption are shown in Figure 9.

According to the results, the Fe_3O_4/NC/MOF reduced the CR concentration from 50.0 to 3.5 mg·L$^{-1,}$ which represents 93% removal efficiency. These findings indicate that the suggested approach might be used effectively, and with a suitable degree of efficiency it removed acid red 88 from a real sample of textile effluent. These results showed that the presence of chemical and biological media, such as dissolved organic nitrogen, had no discernible impact on the dye adsorption processes, and they were quite similar to the removal rates found in synthetic wastewater.

Biodegradability and biological oxygen demand (COD and BOD) were assessed in a real wastewater sample. The amount of dissolved oxidizable organic matter, including non-biodegradable items, was indicated by the COD values. It is clear that a high COD value is frequently linked to wastewater's high organic content, indicating a higher level of ecosystem pollution. BOD is the amount of oxygen needed for organic components in wastewater to break down. From the initial concentration of 1,899 mg·L^{-1}, the COD level dropped to 59 mg·L^{-1}. Parallel to this, the BOD level decreased with time from its initial concentration of 799.0 to 26.0 mg·L^{-1}. This drop in COD and BOD values confirmed the effectiveness of this adsorbent to remove the organic dyes from water. Also, this gives the probability of dye removal from water though the mechanism of molecule breaks down besides the adsorption mechanism. The effectiveness of this adsorbent has been thoroughly assessed, and the treated effluent can be recycled, provided that it is utilized in accordance with the permissible levels of 200.0 and 100.0 mg·L^{-1}, respectively, for irrigation and agricultural purposes. Consequently, the organic part of the dye molecules may be broken down, degraded, or even absorbed during the adsorption process. The above results suggest that Fe_3O_4/NC/MOF might be a good option for real wastewater treatment.

4 Conclusions

In this work, Fe_3O_4/NC was prepared by chemical co-precipitation, and then, under mild conditions, Zn-based MOF was coated by Fe_3O_4/NC utilizing an Et_3N-catalyzed procedure. SEM, FTIR, XRD, XPS, and VSM were used to characterize the resultant Fe_3O_4/NC/MOF material, confirming its effective synthesis. Through a series of extensive tests, the

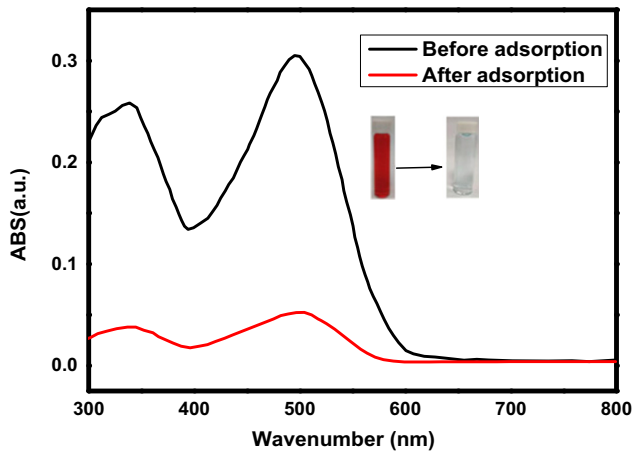

Figure 9: UV spectra before and after adsorption of CR on the surface of Fe_3O_4/NC/MOF.

adsorption conditions of this unique material were adjusted for removing dyes from the aqueous solution. The adsorption process conforms to the Langmuir isotherm model and follows pseudo-second-order kinetics, as indicated by the adsorption data. Regarding CR and BB 54 dyes, we may conclude that their adsorption process onto Fe_3O_4/NC/MOF can be described by both pseudo-first-order and pseudo-second-order models. The adsorption values were fitted to the Langmuir isotherm model, yielding q_m values for the removal of CR, BB 54, BV 14, and AR 88, which were 1248, 999.88, 1248.3, and 1665.89 $mg \cdot g^{-1}$, in that order. The adsorption on Fe_3O_4/NC/MOF was both spontaneous and thermodynamically advantageous, according to the thermodynamic parameters. Fe_3O_4/NC/MOF exhibited endothermic adsorption for AR 88 and exothermic adsorption for CR, BB 54, and BV 14. Subsequently, Fe_3O_4/NC/MOF is an effective dye chelation material that may be applied in a wide range to eliminate pollutants from water because of its special qualities, which include maximum adsorption capacities, high removal efficiency, the number of aromatic rings for π–π interaction, and high recycling capacity.

Acknowledgments: The authors extend their appreciation to the Deanship of Scientific Research at King Khalid University for funding this work through the Large Group Project under grant number RGP.2/174/44. This research was also funded by Princess Nourah bint Abdulrahman University Researchers Supporting Project number (PNURSP2024R19), Princess Nourah bint Abdulrahman University, Riyadh, Saudi Arabia.

Funding information: This research was funded by the Deanship of Scientific Research at King Khalid University under grant number RGP.2/174/44. Additionally, this research was funded by Princess Nourah bint Abdulrahman University Researchers Supporting Project number (PNURSP2024R19), Princess Nourah bint Abdulrahman University, Riyadh, Saudi Arabia.

Author contributions: N.S.A. and H.O. for conceptualization; N.S.A. for methodology; H.O. for software; H.O. for validation; H.O. for formal analysis; N.S.A. for investigation; N.S.A. for resources; A.A. for data curation; H.O. for writing – original draft preparation; N.S.A. for writing – review and editing; A.A. for visualization; M.A.T. for supervision; M.A.T. for project administration; and N.S.A. for funding acquisition. All authors have accepted responsibility for the entire content of this manuscript and approved its submission.

Conflict of interest: The authors state no conflict of interest.

Data availability statement: The datasets generated and/or analysed during the current study are available from the corresponding author on reasonable request.

References

[1] Tkaczyk, A., K. Mitrowska, and A. Posyniak. Synthetic organic dyes as contaminants of the aquatic environment and their implications for ecosystems: A review. *Science of the Total Environment*, Vol. 717, 2020, id. 137222.

[2] Pavithra, K. G. and V. Jaikumar. Removal of colorants from wastewater: A review on sources and treatment strategies. *Journal of Industrial and Engineering Chemistry*, Vol. 75, 2019, pp. 1–19.

[3] Benkhaya, S., S. M'rabet, and A. El Harfi. A review on classifications, recent synthesis and applications of textile dyes. *Inorganic Chemistry Communications*, Vol. 115, 2020, id. 107891.

[4] Mehta, M., M. Sharma, K. Pathania, P. K. Jena, and I. Bhushan. Degradation of synthetic dyes using nanoparticles: A mini-review. *Environmental Science and Pollution Research*, Vol. 28, 2021, pp. 49434–49446.

[5] Nachiyar, C. V., A. Rakshi, S. Sandhya, N. B. D. Jebasta, and J. Nellore. Developments in treatment technologies of dye-containing effluent: A review. *Case Studies in Chemical and Environmental Engineering*, Vol. 7, 2023, id. 100339.

[6] Shen, C., Y. Pan, D. Wu, Y. Liu, C. Ma, F. Li, et al. A crosslinking-induced precipitation process for the simultaneous removal of poly (vinyl alcohol) and reactive dye: the importance of covalent bond forming and magnesium coagulation. *Chemical Engineering Journal*, Vol. 374, 2019, pp. 904–913.

[7] Mcyotto, F., Q. Wei, D. K. Macharia, M. Huang, C. Shen, and C. W. Chow. Effect of dye structure on color removal efficiency by coagulation. *Chemical Engineering Journal*, Vol. 405, 2021, id. 126674.

[8] Ma, J., X. Tang, Y. He, Y. Fan, and J. Chen. Robust stable MoS2/GO filtration membrane for effective removal of dyes and salts from water with enhanced permeability. *Desalination*, Vol. 480, 2020, id. 114328.

[9] Alsaiari, N. S., A. Amari, K. M. Katubi, F. M. Alzahrani, F. B. Rebah, and M. A. Tahoon. The synthesis of magnetic nitrogen-doped graphene oxide nanocomposite for the removal of reactive orange 12 dye. *Adsorption Science & Technology*, Vol. 2022, 2022, pp. 1–14.

[10] Alsaiari, N. S., A. Amari, K. M. Katubi, F. M. Alzahrani, F. B. Rebah, and M. A. Tahoon. Innovative magnetite based polymeric nanocomposite for simultaneous removal of methyl orange and hexavalent chromium from water. *Processes*, Vol. 9, No. 4, 2021, id. 576.

[11] Alsaiari, N. S., A. Amari, K. M. Katubi, F. M. Alzahrani, H. N. Harharah, F. B. Rebah, et al. The biocatalytic degradation of organic dyes using laccase immobilized magnetic nanoparticles. *Applied Sciences*, Vol. 11, No. 17, 2021, id. 8216.

[12] Joseph, J., R. C. Radhakrishnan, J. K. Johnson, S. P. Joy, and J. Thomas. Ion-exchange mediated removal of cationic dye-stuffs from water using ammonium phosphomolybdate. *Materials Chemistry and Physics*, Vol. 242, 2020, id. 122488.

[13] Kumar, V. Adsorption kinetics and isotherms for the removal of rhodamine B dye and Pb+2 ions from aqueous solutions by a hybrid ion-exchanger. *Arabian Journal of Chemistry*, Vol. 12, No. 3, 2019, pp. 316–329.

[14] Velusamy, S., A. Roy, S. Sundaram, and T. Kumar Mallick. A review on heavy metal ions and containing dyes removal through graphene oxide-based adsorption strategies for textile wastewater treatment. *The Chemical Record*, Vol. 21, No. 7, 2021, pp. 1570–1610.

[15] Wang, L., C. Shi, L. Pan, X. Zhang, and J.-J. Zou. Rational design, synthesis, adsorption principles and applications of metal oxide adsorbents: A review. *Nanoscale*, Vol. 12, No. 8, 2020, pp. 4790–4815.

[16] Annamalai, J., P. Murugan, D. Ganapathy, D. Nallaswamy, R. Atchudan, S. Arya, et al. Synthesis of various dimensional metal organic frameworks (MOFs) and their hybrid composites for emerging applications–A review. *Chemosphere*, Vol. 298, 2022, id. 134184.

[17] Li, H., L. Li, R.-B. Lin, W. Zhou, Z. Zhang, S. Xiang, et al. Porous metal-organic frameworks for gas storage and separation: Status and challenges. *EnergyChem*, Vol. 1, No. 1, 2019, id. 100006.

[18] Wang, H. Nanostructure@ metal-organic frameworks (MOFs) for catalytic carbon dioxide (CO2) conversion in photocatalysis, electrocatalysis, and thermal catalysis. *Nano Research*, Vol. 15, No. 4, 2022, pp. 2834–2854.

[19] Alsaiari, N. S., H. Osman, A. Amari, and M. A. Tahoon. The synthesis of metal–organic-framework-based ternary nanocomposite for the adsorption of organic dyes from aqueous solutions. *Magnetochemistry*, Vol. 8, No. 10, 2022, id. 133.

[20] Lu, X. F., Y. Fang, D. Luan, and X. W. D. Lou. Metal–organic frameworks derived functional materials for electrochemical energy storage and conversion: a mini review. *Nano Letters*, Vol. 21, No. 4, 2021, pp. 1555–1565.

[21] Sun, Y., L. Zheng, Y. Yang, X. Qian, T. Fu, X. Li, et al. Metal–organic framework nanocarriers for drug delivery in biomedical applications. *Nano-Micro Letters*, Vol. 12, 2020, pp. 1–29.

[22] Olorunyomi, J. F., S. T. Geh, R. A. Caruso, and C. M. Doherty. Metal–organic frameworks for chemical sensing devices. *Materials Horizons*, Vol. 8, No. 9, 2021, pp. 2387–2419.

[23] Chen, Z., K. O. Kirlikovali, P. Li, and O. K. Farha. Reticular chemistry for highly porous metal–organic frameworks: The chemistry and applications. *Accounts of Chemical Research*, Vol. 55, No. 4, 2022, pp. 579–591.

[24] Zainal-Abidin, M. H., M. Hayyan, J. Matmin, A. M. Al-Fakih, N. Jamaluddin, W. M. A. W. Mahmood, et al. Greening industrial applications with magnetic-based deep eutectic solvents: A promising future. *Journal of Industrial and Engineering Chemistry*, Vol. 124, 2023, pp. 1–16.

[25] Zhang, J., X. Feng, J. Wang, G. Fang, J. Liu, and S. Wang. Nano-crystalline cellulose-coated magnetic nanoparticles for affinity adsorption of glycoproteins. *Analyst*, Vol. 145, No. 9, 2020, pp. 3407–3413.

[26] Farooq, M. U. and M. I. Jalees. Application of magnetic graphene oxide for water purification: Heavy metals removal and disinfection. *Journal of Water Process Engineering*, Vol. 33, 2020, id. 101044.

[27] Tang, Y., S. Zhang, Y. Su, D. Wu, Y. Zhao, and B. Xie. Removal of microplastics from aqueous solutions by magnetic carbon nanotubes. *Chemical Engineering Journal*, Vol. 406, 2021, id. 126804.

[28] Niu, Y., J. Wu, Y. Kang, P. Sun, Z. Xiao, and D. Zhao. Recent advances of magnetic chitosan hydrogel: Preparation, properties and applications. *International Journal of Biological Macromolecules*, 2023, id. 125722.

[29] Muthukumaran, P., P. S. Babu, S. Shyamalagowri, J. Aravind, M. Kamaraj, and M. Govarthanan. Polymeric biomolecules based nanomaterials: production strategies and pollutant mitigation as an emerging tool for environmental application. *Chemosphere*, Vol. 307, 2022, id. 136008.

[30] Hamidon, T. S., R. Adnan, M. M. Haafiz, and M. H. Hussin. Cellulose-based beads for the adsorptive removal of wastewater effluents: A review. *Environmental Chemistry Letters*, Vol. 20, No. 3, 2022, pp. 1965–2017.

[31] Saya, L., Ratandeep, Bikaramjeet, Pooja. *Cellulose-based nanosponges for wastewater remediation. Nanosponges for environmental remediation*, Springer, Switzerland, 2023, pp. 355–382.

[32] Rana, A. K., Y. K. Mishra, V. K. Gupta, and V. K. Thakur. Sustainable materials in the removal of pesticides from contaminated water: Perspective on macro to nanoscale cellulose. *Science of The Total Environment*, Vol. 797, 2021, id. 149129.

[33] Qiao, A., M. Cui, R. Huang, G. Ding, W. Qi, Z. He, et al. Advances in nanocellulose-based materials as adsorbents of heavy metals and dyes. *Carbohydrate Polymers*, Vol. 272, 2021, id. 118471.

[34] Blockx, J., A. Verfaillie, O. Deschaume, C. Bartic, K. Muylaert, and W. Thielemans. Glycine betaine grafted nanocellulose as an effective and bio-based cationic nanocellulose flocculant for wastewater treatment and microalgal harvesting. *Nanoscale Advances*, Vol. 3, No. 14, 2021, pp. 4133–4144.

[35] Wu, Z., S. Xie, Y. Kang, X. Shan, Q. Li, and Z. Cai. Biocompatibility evaluation of a 3D-bioprinted alginate-GelMA-bacteria nanocellulose (BNC) scaffold laden with oriented-growth RSC96 cells. *Materials Science and Engineering: C*, Vol. 129, 2021, id. 112393.

[36] Liu, Y., Q. Fan, Y. Huo, M. Li, H. Liu, and B. Li. Construction of nanocellulose-based composite hydrogel with a double packing structure as an intelligent drug carrier. *Cellulose*, Vol. 28, No. 11, 2021, pp. 6953–6966.

[37] Alzahrani, F. M., A. Amari, K. M. Katubi, N. S. Alsaiari, and M. A. Tahoon. The synthesis of nanocellulose-based nanocomposites for the effective removal of hexavalent chromium ions from aqueous solution. *Open Chemistry*, Vol. 20, No. 1, 2022, pp. 970–983.

[38] Ma, S., M. Zhang, J. Nie, J. Tan, S. Song, and Y. Luo. Lightweight and porous cellulose-based foams with high loadings of zeolitic imidazolate frameworks-8 for adsorption applications. *Carbohydrate polymers*, Vol. 208, 2019, pp. 328–335.

[39] Wang, Z., L. Song, Y. Wang, X.-F. Zhang, D. Hao, Y. Feng, et al. Lightweight UiO-66/cellulose aerogels constructed through self-crosslinking strategy for adsorption applications. *Chemical Engineering Journal*, Vol. 371, 2019, pp. 138–144.

[40] Zhu, H., X. Yang, E. D. Cranston, and S. Zhu. Flexible and porous nanocellulose aerogels with high loadings of metal–organic-framework particles for separations applications. *Advanced materials*, Vol. 28, No. 35, 2016, pp. 7652–7657.
[41] Mahmed, N., O. Heczko, O. Söderberg, and S.-P. Hannula, editors. Room temperature synthesis of magnetite (Fe3− δO4) nanoparticles by a simple reverse co-precipitation Method. *IOP Conference Series: Materials Science and Engineering*, 2011. IOP Publishing.
[42] Khan, I. A., M. Choucair, M. Imran, A. Badshah, and M. A. Nadeem. Supercapacitive behavior of microporous carbon derived from zinc based metal-organic framework and furfuryl alcohol. *International Journal of Hydrogen Energy*, Vol. 40, No. 39, 2015, pp. 13344–13356.
[43] Huang, H., X. Wang, H. Ge, and M. Xu. Multifunctional magnetic cellulose surface-imprinted microspheres for highly selective adsorption of artesunate. *ACS Sustainable Chemistry & Engineering*, Vol. 4, No. 6, 2016, pp. 3334–3343.
[44] Wang, L., G. Chen, H. Shu, X. Cui, Z. Luo, C. Chang, et al. Facile covalent preparation of carbon nanotubes/amine-functionalized Fe3O4 nanocomposites for selective extraction of estradiol in pharmaceutical industry wastewater. *Journal of Chromatography A*, Vol. 1638, 2021, id. 461889.
[45] Lin, X., X. Wang, Q. Zhou, C. Wen, S. Su, J. Xiang, et al. Magnetically recyclable MoS2/Fe3O4 hybrid composite as visible light responsive photocatalyst with enhanced photocatalytic performance. *ACS Sustainable Chemistry & Engineering*, Vol. 7, No. 1, 2018, pp. 1673–1682.
[46] Wang, X., X. Ma, H. Wang, P. Huang, X. Du, and X. Lu. A zinc(II) benzenetricarboxylate metal organic framework with unusual adsorption properties, and its application to the preconcentration of pesticides. *Microchimica Acta*, Vol. 184, 2017, pp. 3681–3687.
[47] Petit, C., B. Levasseur, B. Mendoza, and T. J. Bandosz. Reactive adsorption of acidic gases on MOF/graphite oxide composites. *Microporous and Mesoporous Materials*, Vol. 154, 2012, pp. 107–112.
[48] Ra'ad, Z., L. Al-Karam, and N. A. Alsahib, editors. Synthesis and characterization of dextran coated iron oxide nanoparticles as a T1 contrast agent. *Journal of Physics: Conference Series*, 2021. IOP Publishing.
[49] Hussin, F. N. N. M., N. Attan, and R. A. Wahab. Extraction and characterization of nanocellulose from raw oil palm leaves (Elaeis guineensis). *Arabian Journal for Science and Engineering*, Vol. 45, 2020, pp. 175–186.
[50] Wang, N., R.-N. Jin, A. Omer, and X.-K. Ouyang. Adsorption of Pb(II) from fish sauce using carboxylated cellulose nanocrystal: Isotherm, kinetics, and thermodynamic studies. *International Journal of Biological Macromolecules*, Vol. 102, 2017, pp. 232–240.
[51] Onkarappa, H., G. Prakash, G. Pujar, C. Rajith Kumar, V. Radha, and V. S. Betageri. Facile synthesis and characterization of nanocellulose from Zea mays husk. *Polymer Composites*, Vol. 41, No. 8, 2020, pp. 3153–3159.
[52] Chikri, R., N. Elhadiri, M. Benchanaa, and Y. Maguana. Efficiency of sawdust as low-cost adsorbent for dyes removal. *Journal of Chemistry*, Vol. 2020, 2020, pp. 1–17.
[53] Yagub, M. T., T. K. Sen, S. Afroze, and H. M. Ang. Dye and its removal from aqueous solution by adsorption: a review. *Advances in Colloid and Interface Science*, Vol. 209, 2014, pp. 172–184.
[54] Qiu, B., Q. Shao, J. Shi, C. Yang, and H. Chu. Application of biochar for the adsorption of organic pollutants from wastewater: Modification strategies, mechanisms and challenges. *Separation and Purification Technology*, Vol. 300, 2022, id. 121925.
[55] Mustapha, S., M. Ndamitso, A. Abdulkareem, J. Tijani, A. Mohammed, and D. Shuaib. Potential of using kaolin as a natural adsorbent for the removal of pollutants from tannery wastewater. *Heliyon*, Vol. 5, No. 11, 2019, id. e02923.
[56] Jawad, A. H. and A. S. Abdulhameed. Statistical modeling of methylene blue dye adsorption by high surface area mesoporous activated carbon from bamboo chip using KOH-assisted thermal activation. *Energy, Ecology and Environment*, Vol. 5, No. 6, 2020, pp. 456–469.
[57] Alarifi, I. M., Y. O. Al-Ghamdi, R. Darwesh, M. O. Ansari, and M. K. Uddin. Properties and application of MoS2 nanopowder: Characterization, Congo red dye adsorption, and optimization. *Journal of Materials Research and Technology*, Vol. 13, 2021, pp. 1169–1180.
[58] Sultana, S., K. Islam, M. A. Hasan, H. J. Khan, M. A. R. Khan, A. Deb, et al. Adsorption of crystal violet dye by coconut husk powder: isotherm, kinetics and thermodynamics perspectives. *Environmental Nanotechnology, Monitoring & Management*, Vol. 17, 2022, id. 100651.
[59] Tian, X., R. Yang, T. Chen, Y. Cao, H. Deng, M. Zhang, et al. Removal of both anionic and cationic dyes from wastewater using pH-responsive adsorbents of L-lysine molecular-grafted cellulose porous foams. *Journal of Hazardous Materials*, Vol. 426, 2022, id. 128121.
[60] Ighalo, J. O., S. Rangabhashiyam, C. A. Adeyanju, S. Ogunniyi, A. G. Adeniyi, and C. A. Igwegbe. Zeolitic imidazolate frameworks (ZIFs) for aqueous phase adsorption–a review. *Journal of Industrial and Engineering Chemistry*, Vol. 105, 2022, pp. 34–48.
[61] Mansor, E. S. and T. Aysha. Cerium organic frameworks as green pollution preventing materials for dye removal. *Egyptian Journal of Chemistry*, Vol. 65, No. 131, 2022, pp. 1217–1230.
[62] Alswieleh, A. M. Fabrication of carboxylic functionalized poly (methacrylic acid 2-(tert-butylamino) ethyl ester)-coated mesoporous silica nanoparticles and their application for removing ionic dyes from polluted water. *Heliyon*, Vol. 9, 2023, id. e23180.
[63] Sadiq, A. C., N. Y. Rahim, and F. B. M. Suah. Adsorption and desorption of malachite green by using chitosan-deep eutectic solvents beads. *International Journal of Biological Macromolecules*, Vol. 164, 2020, pp. 3965–3973.
[64] Fatombi, J. K., E. A. Idohou, S. A. Osseni, I. Agani, D. Neumeyer, M. Verelst, et al. Adsorption of indigo carmine from aqueous solution by chitosan and chitosan/activated carbon composite: kinetics, isotherms and thermodynamics studies. *Fibers and Polymers*, Vol. 20, 2019, pp. 1820–1832.
[65] Shokry, H. and H. Hamad. Effect of superparamagnetic nanoparticles on the physicochemical properties of nano hydroxyapatite for groundwater treatment: adsorption mechanism of Fe(II) and Mn(II). *RSC Advances*, Vol. 6, No. 85, 2016, pp. 82244–82259.
[66] Al-Ghouti, M. A. and D. A. Da'ana. Guidelines for the use and interpretation of adsorption isotherm models: A review. *Journal of hazardous materials*, Vol. 393, 2020, id. 122383.
[67] Somashekara, D. and L. Mulky. Sequestration of contaminants from wastewater: a review of adsorption processes. *ChemBioEng Reviews*, Vol. 10, No. 4, 2023, pp. 491–509.
[68] Shikuku, V. O. and T. Mishra. Adsorption isotherm modeling for methylene blue removal onto magnetic kaolinite clay: a comparison of two-parameter isotherms. *Applied water science*, Vol. 11, No. 6, 2021, id. 103.
[69] Saxena, M., N. Sharma, and R. Saxena. Highly efficient and rapid removal of a toxic dye: adsorption kinetics, isotherm, and mechanism studies on functionalized multiwalled carbon nanotubes. *Surfaces and Interfaces*, Vol. 21, 2020, id. 100639.

[70] Alsaiari, N. S., M. S. Alsaiari, F. M. Alzahrani, A. Amari, and M. A. Tahoon. Synthesis, characterization, and application of the novel nanomagnet adsorbent for the removal of Cr (vi) ions. *Reviews on Advanced Materials Science*, Vol. 62, No. 1, 2023, id. 20230145.

[71] Sharifi, M. J., A. Nouralishahi, and A. Hallajisani. Fe_3O_4-chitosan nanocomposite as a magnetic biosorbent for removal of nickel and cobalt heavy metals from polluted water. *International Journal of Biological Macromolecules*, Vol. 248, 2023, id. 125984.

[72] Debnath, S. and R. Das. Strong adsorption of CV dye by Ni ferrite nanoparticles for waste water purification: Fits well the pseudo second order kinetic and Freundlich isotherm model. *Ceramics International*, Vol. 49, No. 10, 2023, pp. 16199–16215.

[73] Hidayat, A. R. P., D. O. Sulistiono, I. K. Murwani, B. F. Endrawati, H. Fansuri, L. L. Zulfa, et al. Linear and nonlinear isotherm, kinetic and thermodynamic behavior of methyl orange adsorption using modulated Al_2O_3@ UiO-66 *via* acetic acid. *Journal of Environmental Chemical Engineering*, Vol. 9, No. 6, 2021, id. 106675.

[74] Harja, M., G. Buema, and D. Bucur. Recent advances in removal of Congo Red dye by adsorption using an industrial waste. *Scientific Reports*, Vol. 12, No. 1, 2022, id. 6087.

[75] Dryaz, A. R., M. Shaban, H. AlMohamadi, K. A. A. Al-Ola, A. Hamd, N. Soliman, et al. Design, characterization, and adsorption properties of Padina gymnospora/zeolite nanocomposite for Congo red dye removal from wastewater. *Scientific Reports*, Vol. 11, No. 1, 2021, id. 21058.

[76] Saleh, S., H. Maarof, S. Rahim, and N. Nasuha. Adsorption of Congo red onto bottom ash. *Journal of Applied Sciences*, Vol. 12, No. 11, 2012, pp. 1181–1185.

[77] Hu, H., J. Liu, Z. Xu, L. Zhang, B. Cheng, and W. Ho. Hierarchical porous Ni/Co-LDH hollow dodecahedron with excellent adsorption property for Congo red and Cr (VI) ions. *Applied Surface Science*, Vol. 478, 2019, pp. 981–990.

[78] Yang, M. and Q. Bai. Flower-like hierarchical Ni-Zn MOF microspheres: Efficient adsorbents for dye removal. *Colloids and Surfaces A: Physicochemical and Engineering Aspects*, Vol. 582, 2019, id. 123795.

[79] Mosavi, S. H., R. Zare-Dorabei, and M. Bereyhi. Rapid and effective ultrasonic-assisted adsorptive removal of congo red onto MOF-5 modified by CuCl2 in ambient conditions: Adsorption isotherms and kinetics studies. *ChemistrySelect*, Vol. 6, No. 18, 2021, pp. 4432–4439.

[80] Suresh, S. Removal of basic violet 14 from aqueous solution using sulphuric acid activated materials. *SpringerPlus*, Vol. 5, No. 1, 2016, pp. 1–14.

[81] Suresh, S., R. W. Sugumar, and T. Maiyalagan. A low cost adsorbent prepared from Curcuma angustifolia scales for removal of Basic violet 14 from aqueous solution. *Indian Journal of Chemical Technology*, Vol. 21, 2014, pp. 368–378.

[82] Gupta, V., A. Mittal, V. Gajbe, and J. Mittal. Adsorption of basic fuchsin using waste materials—bottom ash and deoiled soya—as adsorbents. *Journal of Colloid and Interface Science*, Vol. 319, No. 1, 2008, pp. 30–39.

[83] Konicki, W., I. Pełech, E. Mijowska, and I. Jasińska. Adsorption kinetics of acid dye acid red 88 onto magnetic multi-walled carbon nanotubes-Fe_3C nanocomposite. *Clean–Soil, Air, Water*, Vol. 42, No. 3, 2014, pp. 284–294.

[84] Soltani, R. D. C., A. Khataee, M. Safari, and S. Joo. Preparation of bio-silica/chitosan nanocomposite for adsorption of a textile dye in aqueous solutions. *International Biodeterioration & Biodegradation*, Vol. 85, 2013, pp. 383–391.

[85] Xing, T., H. Kai, and G. Chen. Study of adsorption and desorption performance of acid dyes on anion exchange membrane. *Coloration Technology*, Vol. 128, No. 4, 2012, pp. 295–299.

[86] Venkata Mohan, S., P. Sailaja, M. Srimurali, and J. Karthikeyan. Color removal of monoazo acid dye from aqueous solution by adsorption and chemical coagulation. *Environmental Engineering and Policy*, Vol. 1, 1998, pp. 149–154.

[87] Yang, L., X. Ma, and N. Guo. Sodium alginate/Na+ -rectorite composite microspheres: Preparation, characterization, and dye adsorption. *Carbohydrate Polymers*, Vol. 90, No. 2, 2012, pp. 853–858.

[88] Hou, F., D. Wang, X. Ma, L. Fan, T. Ding, X. Ye, et al. Enhanced adsorption of Congo red using chitin suspension after sonoenzymolysis. *Ultrasonics Sonochemistry*, Vol. 70, 2021, id. 105327.

[89] Sahmoune, M. N. Evaluation of thermodynamic parameters for adsorption of heavy metals by green adsorbents. *Environmental Chemistry Letters*, Vol. 17, No. 2, 2019, pp. 697–704.

[90] Chakraborty, S., A. Mukherjee, S. Das, N. R. Maddela, S. Iram, and P. Das. Study on isotherm, kinetics, and thermodynamics of adsorption of crystal violet dye by calcium oxide modified fly ash. *Environmental Engineering Research*, Vol. 26, No. 1, 2021, id. 190372.

[91] Quesada, H. B., L. F. Cusioli, O. de, C. Bezerra, A. T. Baptista, L. Nishi, et al. Acetaminophen adsorption using a low-cost adsorbent prepared from modified residues of Moringa oleifera Lam. seed husks. *Journal of Chemical Technology & Biotechnology*, Vol. 94, No. 10, 2019, pp. 3147–3157.

[92] Gómez-Avilés, A., M. Peñas-Garzón, C. Belver, J. Rodriguez, and J. Bedia. Equilibrium, kinetics and breakthrough curves of acetaminophen adsorption onto activated carbons from microwave-assisted $FeCl_3$-activation of lignin. *Separation and Purification Technology*, Vol. 278, 2021, id. 119654.

[93] Chen, W., Z. Liu, Q. Tang, B. Du, X. Huang, Y. Mo, et al. Assessment of a novel aminated magnetic adsorbent with excellent adsorption capacity for dyes and drugs. *Journal of Environmental Management*, Vol. 293, 2021, id. 112809.

[94] Fanourakis, S. K., J. Peña-Bahamonde, P. C. Bandara, D. F. Rodrigues. Nano-based adsorbent and photocatalyst use for pharmaceutical contaminant removal during indirect potable water reuse. *NPJ Clean Water*, Vol. 3, No. 1, 2020, id. 1.